

Long-term *Fermi* observations of Mrk 421: clues for different non-stationary processes

B. Kapanadze^{1,2,3}, A. Gurchumelia^{2,4}, M. Aller⁵

Abstract This paper presents the gamma-ray spectral and timing results from the long-term regular observations of Mrk 421 with the Large Area Telescope (LAT) onboard *Fermi* during 2008 August–2023 August. We discerned six periods of the relatively stronger 0.3–300 GeV activity compared to other time intervals. The baseline brightness level varied on timescales from several months to years during these periods, which was superimposed by shorter-term flares of the different asymmetry. The latter are explained by various interplay between the light-crossing, particle acceleration and cooling timescales. The source also frequently exhibited two-peak flares, to be triggered by the propagation of forward and reverse shocks after collision between the "shells" of high-energy plasma, moving with different speeds down the jet. The strongest long-term flaring activity was recorded during 2012 June–2013 October and 2017 October–2018 March when the source was mostly brighter than 10^{-7} ph cm⁻²s⁻¹ in the 0.3–300 GeV energy range and robustly detectable even on intraday timescales. We detected 25 instances of intraday variability and a large number of the flux doubling/halving instances, allowing to constrain the upper limit to the emission zone size to be in the range of 1.3×10^{16} cm– 1.1×10^{18} cm. The source generally showed a lognormal variability in the LAT energy range, explained as an imprinting of the disc nonstationary processes on the jet, proton-initiated hadronic cascades or random

fluctuations in the particle acceleration rate. Most of the 0.3–300 GeV spectra were well-fit with a simple power-law model and showed a very broad range of the photon-index from $\Gamma \sim 2.8$ down to $\Gamma \sim 1.2$, with the mean values $\Gamma_{\text{mean}} = 1.75$ – 1.84 and distribution peaks $\Gamma_p = 1.73$ – 1.82 during the periods of strong LAT-band activity. Our spectral study also revealed the features of inverse-Compton upscatter of X-ray photons in the Klein-Nishina regime, relativistic magnetic reconnection, first-order Fermi mechanism within the magnetic field of different confinement efficiencies and stochastic acceleration.

Keywords (galaxies:) BL Lacertae objects: individual: Mrk 421

1 INTRODUCTION

BL Lacertae objects (BLLs) represent a blazar subclass and exhibit extreme observational features (see, e.g., Begelman et al. 2008): featureless spectra with two broadband SED peaks in the in the νF_ν representation, established by relativistically-boosted non-thermal emission from the jet closely aligned with our line-of-sight (with viewing angles $\theta \lesssim 10$ deg and high bulk Lorentz factor $\Gamma \sim 10$; see, e.g., Falomo et al. 2014); flux variability across the entire electromagnetic range, with different strengths and amplitudes depending on the spectral range; strong and variable radio-to-X-ray polarization; strong γ -ray emission in the high-energy (HE, $E > 1$ MeV) and very-high-energy (VHE, $E > 100$ GeV) bands. These objects are subclassified as low, intermediate and high-energy-peaked BLLs (LBL, IBL and HBLs, respectively), based on the radio-to-X-ray flux ratios (Padovani & Giommi 1995; Bondi 2001). On the other hand, the sequence LBLs→IBLs→HBLs is characterized by the increasing

B. Kapanadze, A. Gurchumelia, M. Aller

¹Ilia State University, Colokashvili Av. 3/5, 0162 Tbilisi, Georgia

²E. Kharadze National Astrophysical Observatory, Mt. Kanobili, 0803 Abastumani, Georgia

³INAF, Osservatorio Astronomico di Brera, Via E. Bianchi 46, 23807 Merate, Italy

⁴I. Javakishvili State University, Chavchavadze Av. 3, Tbilisi 0128, Republic of Georgia

⁵Astronomy Department, University of Michigan, Ann Arbor, MI 48109-1107, USA

synchrotron SED peak (E_p) values, decreasing dominance of the gamma-ray flux over the lower-frequency emission and bolometric luminosity (Böttcher 2007). Note that among the 67 BLLs to be TeV-detected so far, the vast majority are HBLs (84%)¹. Therefore, these sources should comprise highest-energy particles and the most violent acceleration processes (Aharonian et al. 2009).

The lower-energy SED component is firmly explained as synchrotron radiation emitted by ultrarelativistic electrons (and, possibly, positrons) in the magnetized jet medium, owing to the absence of spectral lines and high polarization (Celotti & Ghisellini 2008). However, many problems remain to be solved related to the jet particle content, acceleration and unstable mechanisms. More problems persist with unambiguous identification of the physical mechanisms responsible for the production of the higher-energy SED component, representing γ -rays in HBLs. Currently, two basic mechanisms are most frequently considered: in the leptonic models, ultra-relativistic electron/positron populations perform an inverse Compton (IC) upscatter of their own low-energy synchrotron emission (synchrotron-self-Compton model, SSC; Marscher & Gearhart 1985 and references therein), or the "seed" photons originating from outside the jet (external inverse Compton, EIC; see, e.g., Sikora et al. 1994): thermal emission from the accretion disc (AD), dusty torus, broad-line region (BLR), or from stellar clusters located near the jet emitting region (Cerruti et al. 2015). However, HBLs do not show any significant features inherent to the external photon sources (Aharonian et al. 2009; Plotkin et al. 2012). One-zone SSC scenarios predict a correlated X-ray and VHE variability, especially during strong flares when the emission from a single region is expected to dominate the broadband SED (Aharonian et al. 2009).

Alternatively, hadronic or lepto-hadronic scenarios incorporate specific gamma-ray emission mechanisms to solve the difficulties with the leptonic models (Böttcher & Dermer 2010). Namely, the so-called synchrotron-proton blazar (SPB) model and its modified versions state that the significant portion of the jet kinetic or magnetic power is used to accelerate protons (along with electrons) in a strongly magnetized environment to the threshold of the photo-pion ($p\gamma$) production on the soft photon field, followed by various synchrotron-emitting pair cascades (see, e.g. Mannheim 1993; Aharonian 2000; Cerruti et al. 2020). The lower-energy SED component still is an electron-synchrotron emission (primary and secondary electrons

from the hadronic cascades), while the ultrarelativistic hadron population produces gamma-rays via the synchrotron mechanism. Moreover, the $p\gamma$ -interaction can produce either π^0 or π^\pm mesons. The charged pions subsequently decay into muons and muon neutrinos, whereas muons themselves also decay to produce electrons, positrons, and neutrinos. Consequently, the γ -photons can be emitted from the π^0 -decay process, or by electrons from the $\pi^\pm \rightarrow \mu^\pm \rightarrow e^\pm$ decay (Böttcher et al. 2013). Generally, the proton-emission should contribute to the lower-energy part of the γ -ray SED component, while those from the muon and pion cascades are expected to have higher energies and form the third SED component after the "mutual" higher-energy hump (Cerruti et al. 2015). Finally, the $p\gamma$ -interaction may also result in the Bethe-Heitler pair production as $p + \gamma \rightarrow e^\pm$ (Sol & Zech 2022).

Intense timing/spectral variability studies in different spectral bands and checking for the multi-wavelength (MWL) correlations allow us to discern the viable emission scenario and unstable physical processes operating in blazar jets. These studies are particularly important in the gamma-ray energy range, since this emission is associated with the highest-energy particles, which lose energy very quickly and exist only in the vicinity of the acceleration sites.

Mrk 421 is a nearby ($z=0.031$) HBL source and one of the brightest extragalactic X-ray/TeV objects, providing an unique X-ray space laboratory for solving the aforementioned problems. The *Fermi*-LAT (Atwood et al. 2009) is collecting high-level γ -ray data since 2008 August 5, thus making us capable to perform a detailed timing and spectral study of our target. Mrk 421 was initially included in the *Fermi*-LAT bright gamma-ray source list (0FGL, Abdo et al. 2009a) using the existing LAT observations. The 1.5-yr LAT data revealed a variability up to a factor ~ 3 above 0.3 GeV (Abdo et al. 2011a). During the MWL campaign performed in 2009 January–June, the source showed considerable HE variability uncorrelated with those in other energy ranges (Aleksic et al. 2015a). Aleksic et al. (2015b) used the LAT observations performed in 2010 March for constructing a broadband SED and study MWL correlations. No significant HE variability was detected, contrary to the X-ray and VHE bands. Hovatta et al. (2015) adopted the 2012–2013 LAT data to study the radio- γ -ray cross-correlations, which could exist only for a very specific choice of the model parameters. Abeysekara et al. (2017) did not find any significant variability from the daily-binned 0.1–30 GeV light curve from the time interval 2014 April 28–May 4, and the broadband SED showed the higher-energy peak

¹<http://tevcat.uchicago.edu>

to be below ~ 100 GeV. Balokovic et al. (2016) concluded the LAT-band variability during 2013 January–March to be insignificant. Carnerero et al. (2017) reported a major HE outburst in 2012 and other noticeable flares in 2013 and 2014. Banerjee et al. (2019) found only a mild variability in the *Fermi*–GeV energy range during the strong X-ray and VHE outburst in 2010 February 10–26, while Shukla et al. (2012) reported an intra-day flux variability (IDV) at energies >200 MeV on February 17 (although the light curve clearly shows the variability detection below the commonly accepted 3σ threshold). Acciari et al. (2021) did not find any strong LAT-band flaring episodes during 2016 December–2017 June. The 0.1–300 GeV variability in 2012 December–2018 April was correlated with that observed in the optical and radio energy ranges, although the latter was lagging the GeV-band light curve by 30–100 days (Arbet-Engels et al. 2021). A similar result was obtained by Acciari et al. (2021) for the data collected till 2016 June. The LAT data from the period 2022 April–June (in the epoch of the X-ray polarimetric observations with IXPE) showed a flux variability by a factor of ~ 3 (Abe et al. 2024).

Our past studies of Mrk 421 were mainly focused on the detailed X-ray spectral and timing properties of the source in the epochs of the strong X-ray flaring activity and/or densely-sampled observations with the X-ray Telescope onboard the satellite *Swift* (*Swift*-XRT; Burrows et al. 2005) during 2005 March–2024 December (Kapanadze et al. 2018a,b, 2016, 2017a, 2020, 2024). Our basic findings were as follows: (i) extreme X-ray flaring by a factor of 3–20 on timescales of a few days–weeks; exceptionally strong flares with $\text{CR} > 100 \text{ cts s}^{-1}$ (corresponding to de-absorbed fluxes $F_{0.3-10\text{keV}} \gtrsim 5 \times 10^{-9} \text{ erg cm}^{-2} \text{ s}^{-1}$) which occurred in 2008 June, 2010 February, 2013 April and 2018 January–February. While the TeV-band and X-ray variabilities were mostly correlated (with some exclusions characterized by “orphan” X-ray or TeV-band flares), the source sometimes varied in a complex manner in the MeV–GeV and radio–UV energy ranges (indicating that the MWL emission could not always be generated in a single zone); (ii) flux variability in X-rays and γ -rays showed a lognormal character, possibly indicating that the flux variability to be an imprint of the accretion disk instabilities onto the jet; (iii) extreme X-ray IDV during the strongest flares: flux doubling/halving timescales of 1–7 hr, brightness fluctuations by up to 20% within within a few hundred seconds (possibly related to the small-scale turbulent areas containing the strongest magnetic fields); (iv) the vast majority of the 0.3–10 keV spectra were consistent with the log-parabolic model, which showed relatively

low spectral curvature and correlations between the different spectral parameters (predicted in the case of the first- and second-order Fermi processes). The position of the synchrotron SED peak E_p underwent an extreme variability on diverse timescales between the energies <0.1 keV and >29 keV, with a frequent occurrence of the hard X-ray-peaking spectra in higher states (rarely observed in BLLs). The photon index showed very hard values on some occasions, hinting at the possible presence of a jet hadronic component; (v) very fast transitions of logparabolic-to-powerlaw spectra, most plausibly caused by turbulence-driven relativistic magnetic reconnection (RMR).

The aforementioned MWL campaigns were triggered in the epochs of enhanced X-ray and TeV-band activity, and, consequently, these studies are biased towards the high states of the source. On the contrary, the LAT-band timing and spectral properties in the intermediate and low γ -ray states have been poorly presented in the literature. Since the spectral properties of Mrk 421 in the MeV–GeV energy range was studied by a few authors in the restricted time span, no statistical treatment of the spectral properties and the corresponding physical implications are provided. By expanding our study on the 15-yr period of the LAT operations (2008 August–2023 August), we have investigated the timing and spectral properties of Mrk 421 on various timescales. Our results are based only on the robust detections of the source with LAT, contrary to some previous studies which also included the data from the 100–300 MeV band (not recommended for HBL sources). Our experimental results have been compared with those obtained in the framework of the recent theoretical studies and simulations, allowing us to draw conclusions about the unstable physical processes operating in the target’s jet. For this purpose, we also checked for the interplay between the 0.3–300 GeV flux variability and those observed in other spectral ranges with different instruments: the First G-APD Cherenkov Telescope (FACT; Anderhub et al. 2013); *Swift*-XRT, the Ultraviolet-Optical Telescope (UVOT; Roming et al. 2005) and the Burst Alert Telescope (BAT; Barthelmy et al. 2005) onboard *Swift*, MAXI (Matsuoka et al. 2009), different ground-based optical and radio telescopes.

The paper is organized as follows: Section 2 encompasses the description of the data processing and analyzing procedures. Section 3 is devoted to the results of the 0.3–300 GeV timing study and the contemporaneous MWL variability of Mrk 421. The MeV–GeV spectral properties and variability are provided in Section 4. We discuss physical implications from our experimental results and draw the corresponding conclusions in

Table 1 Summary of the LAT observations of Mrk 421 during 2008 August–2023 August. For each time integration, the maximum, minimum and mean fluxes (Cols. 2, 3 and 4, respectively) and fractional variability amplitude (in percents; Col. 5) are provided.

Band (units) (1)	Maximum (2)	Minimum (3)	Mean (4)	F_{var} (5)
LAT 0.3–300 GeV (2 weeks, $10^{-8}\text{ph cm}^{-2}\text{s}^{-1}$)	30.70(1.95)	1.91(0.57)	7.19(0.04)	40.3(0.6)
LAT 0.3–300 GeV (1 week, $10^{-8}\text{ph cm}^{-2}\text{s}^{-1}$)	32.47(2.33)	1.92(0.33)	6.94(0.04)	43.3(0.5)
LAT 0.3–300 GeV (4 d, $10^{-8}\text{ph cm}^{-2}\text{s}^{-1}$)	37.74(4.86)	1.83(0.61)	6.71(0.04)	45.6(0.5)
LAT 0.3–300 GeV (3 d, $10^{-8}\text{ph cm}^{-2}\text{s}^{-1}$)	40.09(6.85)	2.00(0.64)	6.69(0.04)	46.2(0.5)
LAT 0.3–300 GeV (2 d, $10^{-8}\text{ph cm}^{-2}\text{s}^{-1}$)	42.40(3.63)	2.27(0.87)	7.11(0.04)	43.4(0.5)
LAT 0.3–300 GeV (1 d, $10^{-8}\text{ph cm}^{-2}\text{s}^{-1}$)	50.21(5.54)	3.17(0.76)	9.12(0.05)	37.2(0.5)

Section 5. Finally, the summary of our study is given in Section 6.

2 DATA REDUCTION and ANALYSIS

The LAT data of Mrk 421 were retrieved from the *Fermi* data server² and processed by using the software *Science Tools* (version 2.2.0, provided by the Fermi-LAT collaboration³). We followed the standard procedure provided by the Fermi Science Support Center⁴ (FSSC). Namely, the instrument response function `P8R3_SOURCE_V2` and the maximum likelihood method `GTLIKE`⁵ were adopted. In order to extract the photon flux and spectral information, we selected the 0.3–300 GeV energy range due to the following reasons: (i) the LAT effective area is larger ($>0.5\text{m}^2$); (ii) the angular resolution is relatively good in this energy range (the 68% containment angle smaller than 2 versus 3.5 at 100 MeV); (iii) minimize contamination from misclassified cosmic rays (Atwood et al. 2009). Therefore, there are smaller systematic errors and the spectral fit is less sensitive to possible contamination from unaccounted, transient neighbouring sources (Abdo et al. 2011a).

The events of the “diffuse” class (`evclass=128`, `evtype=3`) (i.e. those with the highest probability of being photons) from a region of interest (ROI) with the 10-deg radius centered at the location of Mrk 421 were included in our analysis. The data were filtered by using the `gtselect` and `gtmktime` tools included in the aforementioned software: (a) events at zenith angles >90 deg were discarded to avoid a contamination from the Earth-albedo photons, generated by cosmic rays interacting with the upper atmosphere; (b) photons recorded when the spacecraft’s rocking angle was larger

than 52 deg were removed that greatly reduced the contamination from Earth-limb photons; (c) time intervals with poor data quality, flagged as anything other than “Good” were also excluded. A background subtraction was performed by means of the XML model file, created by using the Python application `make4FGLxml.py` and incorporating: (i) the Galactic diffuse-emission component; (ii) the isotropic component, which is the sum of the extragalactic diffuse emission and the residual charged particle background; (iii) all γ -ray sources from the 4FGL catalogue within the 20 deg radius from Mrk 421. For the spectral modelling of our target in the entire 0.3–300 GeV energy range, we adopted the log-parabola model (Massaro et al. 2004), similar to the catalogue:

$$dN/dE = K(E/E_0)^{-[\alpha+\beta\log(E/E_0)]}, \quad (1)$$

with E_0 the reference energy; α , the photon index at the energy E_0 ; β , measures the curvature around the peak; K , the normalization factor. However, most of the spectra obtained via the different time integrations (from two weeks down to intraday timescales) did not show a significant curvature (detection below the 2σ significance). In such a situation, we re-launched the `GTLIKE` tool by adopting a simple power-law model $F(E) = KE^{-\Gamma}$, with Γ , the photon index throughout the entire energy range, and the 0.3–300 GeV photon flux was derived along with the Γ -value.

The spectral parameters of the sources within the ROI were left free during the minimization process, while those outside of this range were held fixed to the 4FGL catalog values (according to the common practice; see, e.g., Acciari et al. 2021). In order to reduce systematic uncertainties in the analysis, the photon index of the isotropic component and the normalization of both components were fixed (see Abdo et al. 2011b). The light curves were generated using the time bins of different duration, repeating the likelihood analysis for each interval. In each case, the photon flux, photon index, curvature parameter, test-statistics (TS) and the number of the model-predicted photons N_{pred} of the

²<https://fermi.gsfc.nasa.gov/ssc/data/access/>

³<http://fermi.gsfc.nasa.gov/>

⁴<https://fermi.gsfc.nasa.gov/ssc/data/analysis/>

⁵http://fermi.gsfc.nasa.gov/ssc/data/analysis/documentation/Cicerone/Cicerone_Likelihood

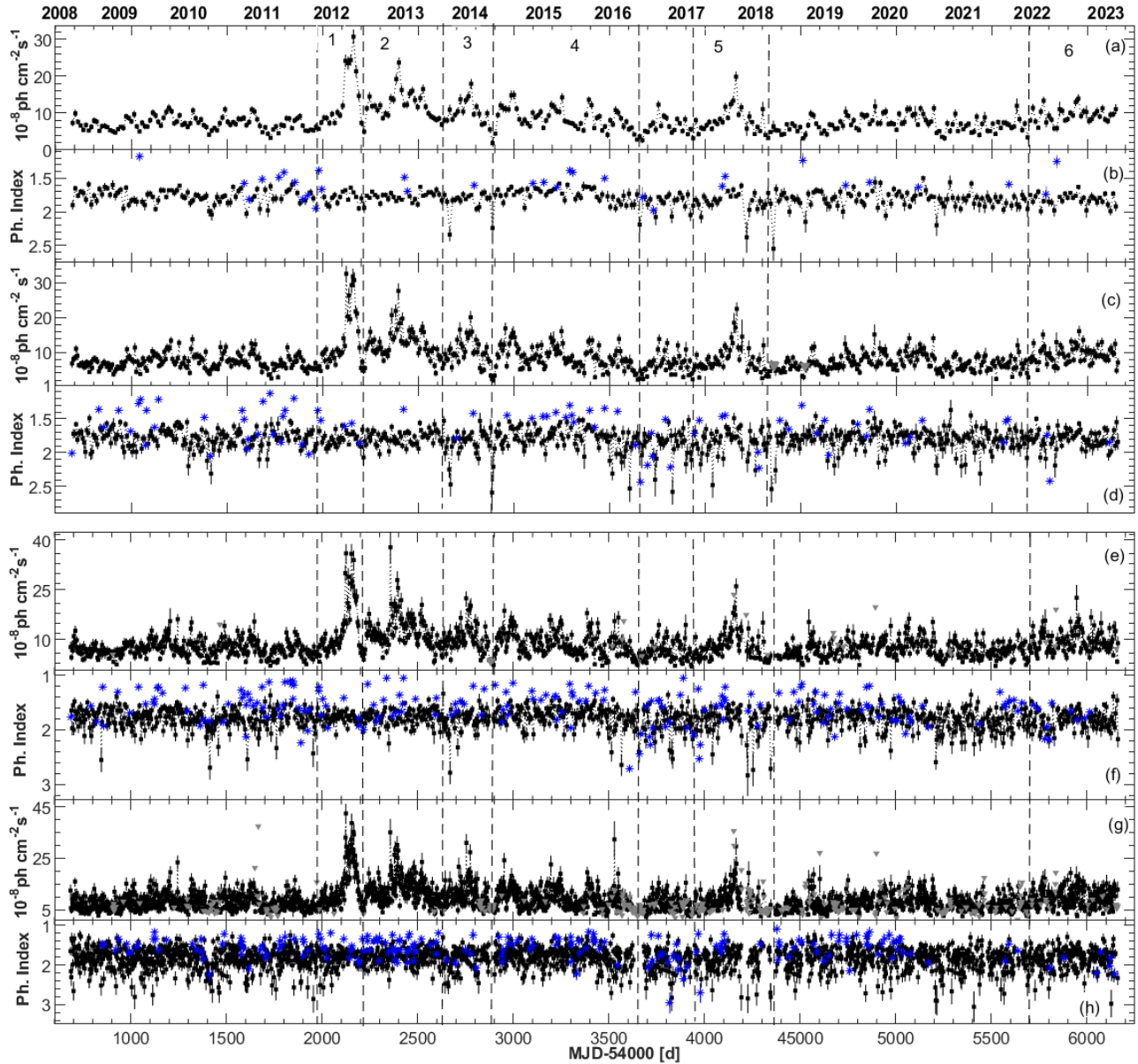


Fig. 1 0.3–300 GeV photon flux and indices plotted versus time by using various time bins: panels (a)–(b): 2 weeks; (c)–(d): 1 week; (e)–(f): 4 days; (g)–(h): 2 days. The power-law and logparabolic photon indices are plotted with black points and blue asterisks, respectively. The downward gray triangles show the upper limits to the 0.3–300 GeV flux when $TS < 9$ and/or $N_{\text{pred}} < 8$. The vertical dashed line denotes a boundary between the different time intervals listed in Table 2.

source were determined. The target’s detection significance is $\sqrt{TS}\sigma$ (Abdo et al. 2009b). In order to have the target’s robust detection, we employed the 3σ threshold. Moreover, when the number of the model-predicted counts $N_{\text{pred}} \lesssim 8$, such a detection is not robust. For example, even a small change in the time-bin width can result in significantly different values of the photon flux and spectral parameters. In such cases, we calculated the upper limit to the photon flux⁶.

The source was monitored by the FACT telescope (Observatorio del Roque de los Muchachos, La Palma, Spain; Anderhub et al. 2013) in the VHE range during the period of our study till the end of 2021 June, followed by the period of seasonal ”invisibility”, volcano eruption at La Palma and its aftermaths, as well as by some technical problems⁷. The FACT collaboration published the results of a quick-look analysis promptly

⁷<http://www.fact-project.org>

⁶According to the recipe provided on fermi.gsfc.nasa.gov/ssc/data/analysis/scitools/upper_limits.html

Table 2 Summary of the LAT-band of Mrk 421 in different periods. The maximum, minimum and mean LAT-band flux values (Columns 4, 5 and 6, respectively) are derived from one-weekly integrated LAT data and given in units of $10^{-8} \text{ph cm}^{-2} \text{s}^{-1}$; fractional variability amplitude (Col. 7) – in per cent.

Per. (1)	Dates (UTC) (2)	MJDs (3)	F_{max} (4)	F_{min} (5)	F_{mean} (6)	F_{var} (7)
1	2012-03-01–10-15	55988–56216	32.47(2.33)	4.62(0.70)	14.04(0.23)	60.4(1.8)
2	2012-10-17–2013-10-25	(56)216–589	27.54(2.24)	3.93(0.88)	12.89(0.18)	51.7(1.5)
3	2013-10-26–2014-08-19	(56)590–888	20.03(1.83)	2.25(0.80)	9.40(0.19)	36.3(2.1)
4	2014-08–20–2016-09-18	56889–57649	16.79(1.70)	1.91(0.69)	8.46(0.10)	34.8(1.6)
5	2017-07-03–2018-07-25	57938–58325	22.41(1.86)	2.20(0.63)	7.85(0.16)	47.9(2.2)
6	2022-06-01–2023-08-01	59696–60157	16.01(1.58)	2.80(0.72)	9.50(0.14)	33.6(1.7)

after each observation⁸. Generally, the background-subtracted VHE excess rates are not corrected for the effect of changing energy threshold with various zenith distances and ambient light (Dorner et al. 2015). However, we restricted our study only to the nights with a signal detected with a minimum significance of 3σ . In this case, more than 98% of the FACT data are obtained with zenith distances small enough to not significantly influence the energy threshold of the analysis. Nevertheless, more than 84% of these data are taken under light conditions which do not increase the analysis threshold (see, e.g., Kapanadze et al. 2020).

We also collected the publicly available MWL data from the sources as follows: (a) the long-term Whipple data included on the VERITAS website⁹ (originally published by Acciari et al. (2014)); (b) the X-ray, UV, optical and radio data from our past studies (Kapanadze et al. 2016, 2017a, 2018a,b, 2020, 2024), the AAVSO International Database¹⁰, University of Michigan Radio Astronomy Observatory (UMRAO) database¹¹ and Large VLBA Project BEAM-ME program¹²; (c) the background-subtracted 2–20 keV data obtained with *MAXI*, which are publicly available on the mission’s website¹³. As customary for the coded-mask devices, the retrieved, 1-d binned data was filtered by adopting the 5σ detection threshold. However, we also plotted the 2–20 keV fluxes corresponding to the detections with $(3\text{--}4)\sigma$ significances for discerning the time intervals of relatively enhanced hard X-ray activity of the target. Furthermore, we used the 15–150 keV *Swift*-BAT data retrieved from the web-

site of the Hard X-ray Transient Monitor program¹⁴ (Krimm et al. 2013). Since the target was relatively rarely detectable with 5σ significance (the BAT also to be a coded-mask device; see, e.g., Barthelmy et al. 2005), we re-binned the orbit-resolved BAT data via the HEASOFT task REBINGAUSSLC, using the 1-week integration.

3 The LAT-band flux Variability on Various Timescales

3.1 Overall 0.3–300 GeV variability

Generally, Mrk 421 is the brightest LAT-band source among the HBL objects and detectable even on intraday timescales during the strong HE γ -ray flares. The LAT-band light curves constructed by using the different time integrations (from 2 weeks down to 2 d) are presented in Figure 1. In the period of our study, the source was not detectable with the LAT from the two-week binned 0.3–300 GeV data only once: it was not observed during 2018 March 20–April 9 [MJD (58)197–217] and, therefore, no good time intervals (GTIs) were available. This time interval corresponded to three bins in the case of the one-weekly integrated data, and there were another three occasions corresponding to the target’s detection below the 3σ threshold from the 1-week-binned data, after adopting the filtering criteria described in Section 2.1. In the case of the shorter integration times, Mrk 421 was detected with a significance of at least 3σ and $N_{\text{pred}} \gtrsim 8$ for 95, 90, 86 and 51 per cents of the 4, 3, 2 and 1-day bins, respectively. A summary of the corresponding light curves is provided in Table 1, presenting the maximum, minimum and mean values of each data train. Using the standard χ^2 -test, we define a source as variable if the probability that its flux is constant is less than 10^{-3} . The last column presents the

⁸See <http://www.fact-project.org/monitoring>

⁹<http://veritas.sao.arizona.edu/veritas-science/mrk-421-long-term-lightcurve>

¹⁰<https://www.aavso.org/aavso-international-database>

¹¹<http://dept.astro.lsa.umich.edu/datasets/umrao.php>

¹²<https://www.bu.edu/blazars/BEAM-ME.html>

¹³<http://maxi.riken.jp>

¹⁴<http://swift.gsfc.nasa.gov/results/transients/weak/Mrk421>

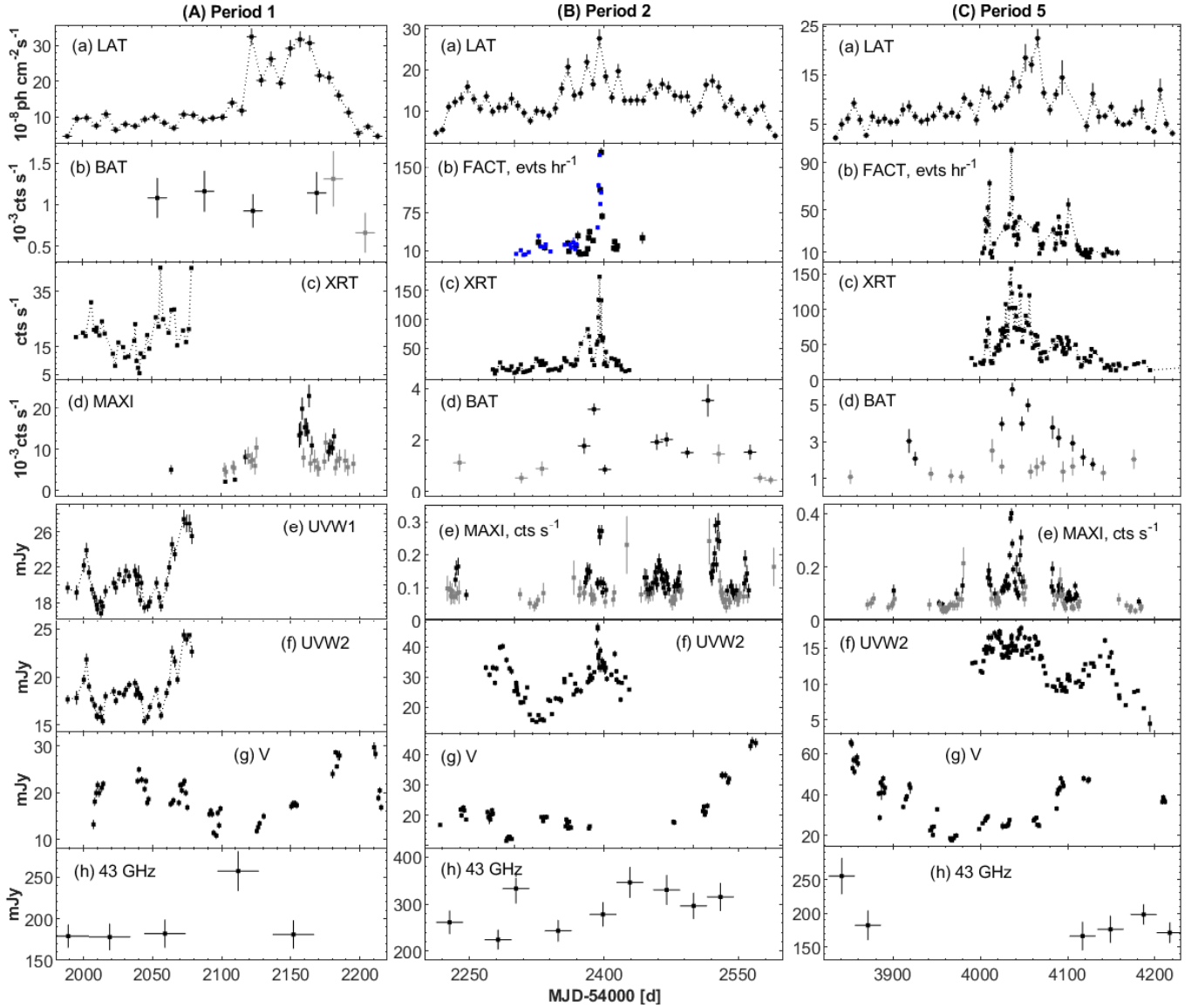


Fig. 2 MWL light curves in the periods listed in Table 2. While the XRT, MAXI, FACT, UVOT, V -band and UMRAO data (next page) data are plotted by using the 1-d integration, the BAT and LAT light curves are based on data binned every one week. The 43 GHz data are obtained approximately monthly. In the panels with the BAT and MAXI-band light curves, the black and grey data points correspond to the detections of Mrk 421 with 5σ and $(3-4)\sigma$ significances, respectively. In Period 2, the blue points in the second panel from the top correspond to the VHE flux values from the observations with the different Cherenkov-type telescopes (originally provided in the different units and multiplied by the corresponding numbers to make compatible with the FACT results presented in events hr^{-1}).

fractional variability amplitude and its error as follows (Vaughan et al. 2003):

$$F_{\text{var}} = (S^2 - \overline{\sigma_{\text{err}}^2})^{1/2} / \overline{F} \quad (2)$$

with S^2 , the sample variance; $\overline{\sigma_{\text{err}}^2}$, the mean square error; \overline{F} , the mean flux. We see that the 0.3–300 GeV photon flux frequently was higher than the level of $10^{-7} \text{ph cm}^{-2} \text{s}^{-1}$. Note that such states has been very rarely observed for other HBLs.

The highest historical 0.3–30 GeV flux of about $10^{-6} \text{ph cm}^{-2} \text{s}^{-1}$ was recorded on 2013 April 15, during the two subsequent 1-hr segments [MJD 56397.(33–42)]. However, the source was not detected securely above this threshold, taking into account the associated uncertainties. Note that Mrk 421 was detectable during the even shorter, 0.6-hr time interval on 2012 July 16 [MJD (56124.)47–50] coinciding with the strongest MeV–GeV band activity of Mrk 421 since the start of *Fermi* operations (see below).

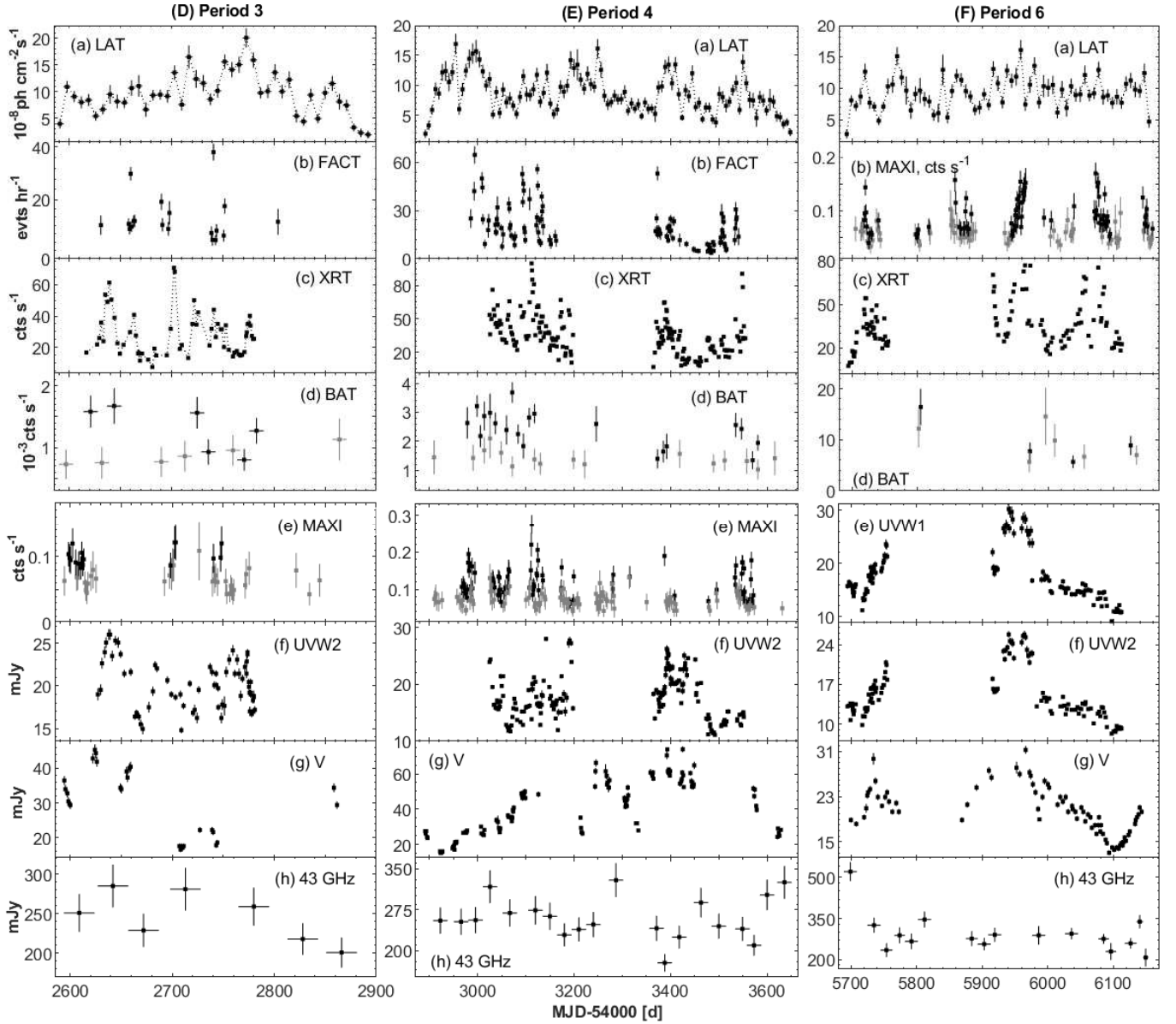


Fig. 2 - Continued.

Based on the maximum 0.3–300 GeV flux and fractional variability amplitude from the weekly binned data, we have discerned six periods of the relatively stronger LAT-band activity compared to other time intervals from the entire 2008 August–2023 August period (see Table 2 for the summary). During these periods, the baseline flux level (defined by the curve connecting the lowest states of short-term flares) was generally higher than that in other epochs, showing a long-term increase and subsequent decline trends on a few months to yearly timescales. Below, we characterize each period in order of the descending values of F_{max} and F_{var} .

3.2 Periods of strong LAT-band activity

The source underwent the strongest LAT-band flaring activity in the second half of Period 1, which lasted about 3 months (2012 June–September, MJD (56)080–200; Figure 2A) and was characterized by the highest historical 0.3–300 GeV flux in the case of the time integrations of 1 d and longer (listed in Table 1). This outburst was preceded by a plateau-like behaviour during ~ 100 d when the source showed minor fluctuations around the mean level of $9 \times 10^{-8} \text{ ph cm}^{-2} \text{ s}^{-1}$. On the other hand, the latter was a factor of ~ 2.5 higher than the 0.3–300 GeV flux observed in the period’s start and about 30 per cent higher than the mean level from all LAT observations of Mrk 421 performed before

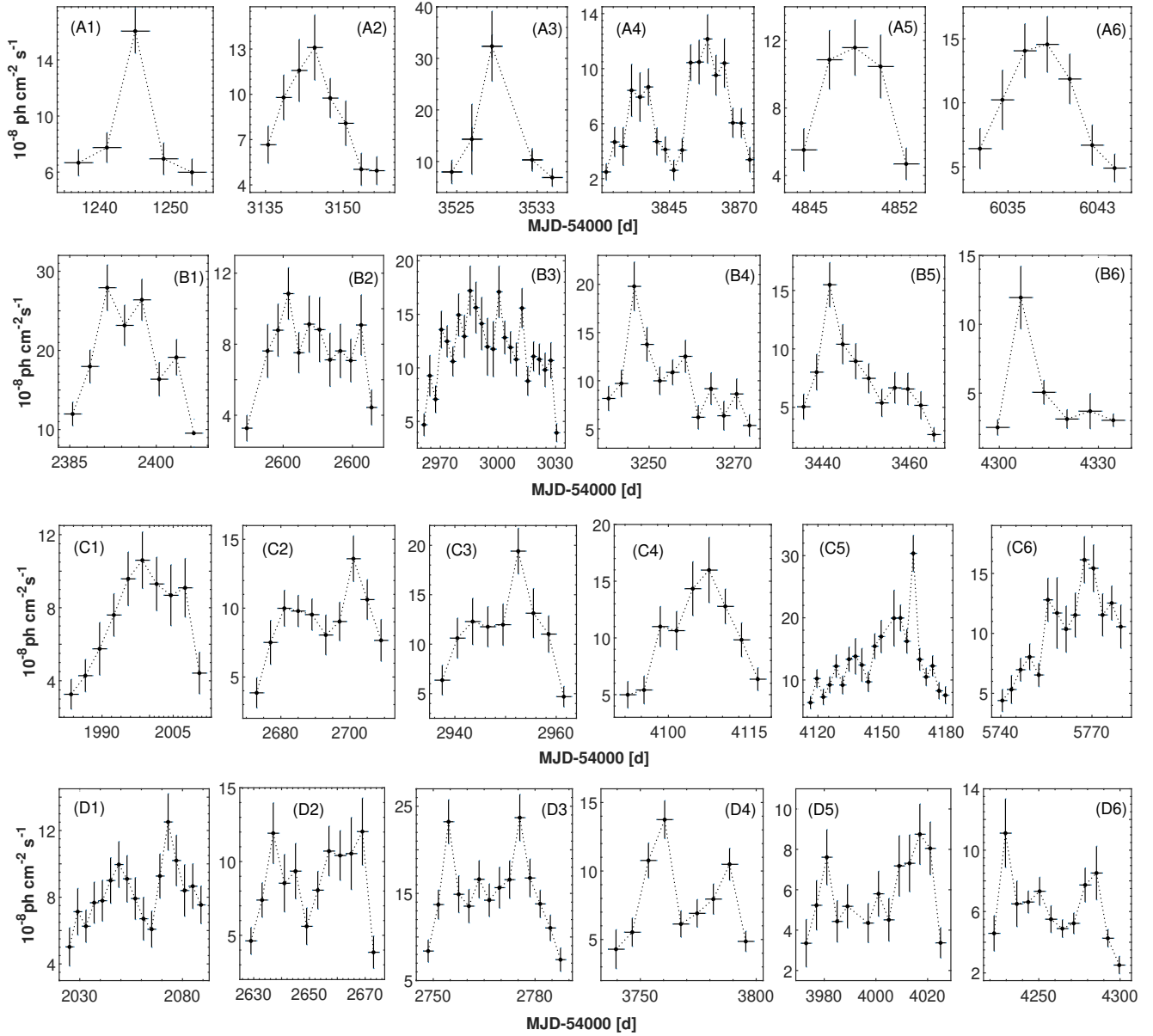


Fig. 3 Examples of short-term LAT-band flares with different profiles: symmetric (A); positively (B) and negatively (C) asymmetric; two-peak (D). The light curves of the different instances are constructed by means of the 0.3–300 GeV flux values derived with 2-d to 1-week time integrations.

2012 March. During the strongest LAT-band activity, the source showed a nearly-symmetric short-term flare by a factor of ~ 2 lasting more than 2 weeks. In this period, the source also underwent two short-term flares with a positive asymmetry (i.e., fast brightness increase and slower decline) and three other flares with a negative asymmetry (an opposite cadence; see Figure 3 for the corresponding examples and Table 3 for the maximum and mean flux values, maximum-to-minimum flux ratio and F_{var}). Finally, the source exhibited two other LAT-band flares of 1-2 months duration, showing a two-peak profile (see Figure 3D for examples and Section 5.2

for the corresponding physical implication). Moreover, 11 instances of the 0.3–300 GeV flux doubling or halving occurred in the course of the aforementioned flares, and the corresponding summary (maximum duration Δt , initial and final flux values, F_{var} , doubling/halving timescale $\tau_{\text{d,h}}$). Note that the quantity $\tau_{\text{d,h}}$ was calculated as follows (Saito et al. 2013)

$$\tau_{\text{d,h}} = \Delta t \times \ln(2) / \ln|(F_{\text{f}}/F_{\text{i}})|, \quad (3)$$

with F_{i} and F_{f} to be the initial and final flux values, respectively, and Δt , the corresponding maximum duration. For these instances, $\Delta t = 0.33\text{--}15$ d, yielding a

Table 3 Summary of shorter-term flares with the time ranges provided in Col. 1 (extract). The maximum and mean 0.3–300 GeV flux values (Columns 2 and 3, respectively) are given in units of 10^{-8} ph cm $^{-2}$ s $^{-1}$; maximum-to-minimum flux ratio (Col. 4); reduced Chi-squared and the corresponding degrees-of-freedom (Col. 5) and fractional rms variability amplitude (Col. 6; in percents); integration time used for the light curve construction (Col. 7).

MJDs (1)	F_{\max} (2)	F_{mean} (3)	\mathfrak{R} (4)	χ_r^2/DOF (5)	F_{var} (6)	Binning (7)
Symmetric flares						
(54)686–720	14.72(1.85)	7.24(0.37)	3.8(0.9)	3.11/13	28.7(5.4)	3 d
(547)50–57	8.28(1.38)	4.91(0.53)	2.1(0.5)	6.92/2	40.2(10.8)	4 d
(548)46–52	10.57(1.54)	5.81(0.76)	6.9(2.1)	6.75/2	56.0(12.7)	3 d
(550)22–47	7.72(1.20)	4.83(0.34)	3.0(0.8)	4.76/8	25.8(6.4)	3 d

range $\tau_{\text{d,h}}=0.21\text{--}9.65$ days (see Table 4 for details). The most extreme instance was recorded on 2012 August 6 (MJD 56145) when the 0.3–300 GeV brightness boosted by a factor of ~ 3 in 8 hr ($\tau_{\text{d}}=5.04$ hr; see Figure 4a). Subsequently, the brightness declined by at least 29% within the next 8 hr (taking into account the flux error ranges; see also Table 5). Another extreme instance with $\tau_{\text{h}}=12$ hr occurred during 2012 July 27–28 when the HE brightness dropped by a factor of ~ 4 within one day [MJD (56)135.5–136.5; Figure 4b)], and this behaviour was preceded by a flux increase by at least 38% within the same time interval.

The source showed a brightness drop by a factor of 3 within 16 hr on August 28–29 [MJD (561)67.67–68.33; see Table 5]. A comparable drop occurred also during MJD (561)19.5–20.5 (2012 July 11–12; $\tau_{\text{h}}\approx 14.5$ hr; Figure 4c), which was preceded by a flux-doubling instance with $\tau_{\text{d}}=3.18$ d (see Table 4). The subsequent HE intraday variability (IDV) occurred on July 16 (MJD 56124) when the brightness increased by more than 70% within the time interval shorter than 1 d, followed by a flux halving during the next 3 days. A flux-halving instance with $\tau_{\text{h}}\approx 14.5$ hr occurred also within MJD (5616)1.5–2.5 (2012 August 21–22), which was followed by a LAT-band IDV after 1 d (see Figure 4d and Table 4). Finally, another instance is detected from LAT data collected during the last 8-hr segment of 2012 August 15 (MJD 56154) when the 0.3–300 GeV brightness dropped by more than 35% (Figure 4e). However, the latter was also preceded by a flux-doubling instance with $\tau_{\text{d}}=1.71$ d.

Unfortunately, no XRT and UVOT observations were performed in the course of the LAT-band outburst of Mrk 421, owing to the seasonal Sun restriction during June–October¹⁵. The regular BAT-band observations yielded only two detections with 5σ significance meanwhile, showing relatively low 15–150 keV states of the source. However, an X-ray flare was detected with MAXI in the epoch of the second 0.3–300 GeV peak,

in contrast to the first, higher peak (accompanied by enhanced radio-band activity; see the last panel of Figure 2A). Moreover, that flare was relatively moderate compared to those detected in Periods 2 and 4–5 (see Figures 2B–2C and 2E). As for the time interval with the plateau-like HE behaviour of the source, the XRT observations mostly showed low 0.3–10 keV states (see the 3-rd panel in Figure 2A). A strong flare was observed in the *UVW1–UVW2* bands around MJD 56075, which was weaker in the optical *V*-band [panels (e)–(g)]. Finally, the source was not observed with FACT or other Cherenkov-type telescopes during the entire period.

The source showed another LAT-band outburst in 2013 March–April [MJD (56)350–410, Period 2], when the exceptionally strong 0.3–10 keV flare occurred (Figure 2B). A similar behaviour was observed also with FACT and UVOT. However, Mrk 421 was relatively quiet in the hard X-ray bands (as observed by BAT and MAXI), and a stronger MAXI-band activity was recorded about 1 month later [panel (e)]. Note that the relatively high 0.3–300 GeV flux (exceeding the threshold of 10^{-7} ph cm $^{-2}$ s $^{-1}$) was observed during most parts of Period 2. On weekly timescales, the source showed five symmetric flares with $F_{\text{var}}=25\text{--}29$ per cent. Moreover, this period was characterized by five positively and one negatively-asymmetric instances, as well by three two-peak flares (see Table 3). Note that the short-term 0.3–300 GeV flare in the epoch of the X-ray outburst showed a positive asymmetry, whereas it was preceded by the symmetric and positively-asymmetric flares, respectively. The source underwent another strong UV-flare centered on MJD 56287 and showing no corresponding LAT-band, X-ray and optical “counterparts”. Nevertheless, the strongest optical *V*-band flare was observed at the period’s end, when the 0.3–300 GeV brightness was showing a long-term declining trend.

The source also showed 16 instances of the LAT-band flux doubling/halving with $\tau_{\text{d,h}}=0.6\text{--}7.4$ d and $F_{\text{var}}=32.6(5.4)\text{--}74.0(10.6)$ per cent during that period (Table 4). The most extreme variability was observed

¹⁵See <https://www.swift.ac.uk/sunpos.php>

Table 4 Summary of the 0.3–300 GeV flux doubling/halving instances (extract). Column (1) gives the maximum duration of the particular instance (in days). The initial and final flux values (in $10^{-8}\text{ph cm}^{-2}\text{s}^{-1}$), reduced Chi-squared along with the corresponding degrees-of-freedom and fractional rms variability amplitude (in percents) are provided in Cols. 4–7, respectively.

Δt (d)	MJDs	Date(s)	F_i	F_f	χ_r^2/DOF	F_{var}
(1)	(2)	(3)	(4)	(5)	(6)	(7)
5	(5470)3–7	2008 Aug 25–29	7.01(1.73)	23.21(2.93)	8.01/3	45.5(8.7)
8	(547)09–16	2008 Aug 29–Sep 5	15.94(2.02)	5.39(1.10)	11.37/3	46.7(7.5)
8	(548)29–36	2008 Dec 29–2009 Jan 5	2.67(0.75)	9.16(1.36)	6.63/3	46.6(10.1)
6	(550)17–22	2009 Jul 5–10	15.04(2.36)	3.99(0.86)	9.94/2	62.8(12.8)

on 2013 April 15 (MJD 56397), when the 0.3–300 GeV flux dropped by a factor of ~ 3 within the 14.5 hr time interval after the interval’s highest brightness (Figure 4f). This instance was preceded by another IDV, incorporating a brightness increase by more than 50% (see Table 5). Three other IDVs were respectively characterized by: (1) a brightness drop by at least 32% within the first half of 2013 March 26 (MJD 56377; Table 5); (2) a brightening by $\sim 80\%$ and subsequent drop to the initial level, with the entire cycle lasting 1.5 d [April 10–11; MJD (5639)2.0–3.5; Figure 4f]; (3) a brightness increase by more than 64% within the first half of 2013 August 9 (MJD 56513). Note that this period included the aforementioned two 1-hr robust detections of the source with the 0.3–300 GeV flux of $\approx 10^{-6}\text{ph cm}^{-2}\text{s}^{-1}$.

Very strong 0.3–300 GeV activity was recorded also in the middle of Period 5, reaching a level of $3 \times 10^{-7}\text{ph cm}^{-2}\text{s}^{-1}$ during the negatively-asymmetric flare peaking on MJD 58166 (see Figures 2C and 3Cf). This instance was preceded by another short-term flare with a negative asymmetry, whereas two flares with opposite asymmetry, two symmetric and three two-peak flares occurred in the same period (see Table 3). At the onset of the aforementioned highest-peak flare, the source also underwent a very strong VHE outburst by a factor of ~ 10 , which showed a peak brightness about one month earlier than the LAT-band flare. Note that the peak VHE brightness during this instance was comparable to that observed in 2013 April. There was another very strong FACT-band flare by a factor of 8, peaking on MJD 58111 (in 8 d) and followed by a very fast drop to the initial brightness (in 2 d). During this time window, only a low-amplitude HE flare was recorded with LAT. However, the source showed a strong γ -ray flare in the both LAT and FACT bands around MJD 58200, when the VHE emission boosted by a factor of ~ 3 . This flare was not accompanied by the comparable XRT-band activity, in contrast to the previous VHE instances when the 0.3–10 keV flux exceeded the threshold of 150cts s^{-1} (the second highest

level after the exceptionally strong X-ray outburst in 2013 April). These fast instances were superimposed on the long-term flare lasting ~ 4 months, which was also recorded with LAT, BAT, MAXI and UVOT. However, the source showed lower optical brightness in the epoch of the highest UV to VHE states, and it underwent a flare during the long-term declining trend in the LAT band. Note also the strongest V-band flare and elevated 43 GHz in the period’s start when the source underwent a negatively-asymmetric LAT-band flare by a factor of ~ 4 . In this period, the source showed a flux doubling/halving ten times, generally occurring during the aforementioned short-term LAT-band flares (Table 4). During one of these instances, the source underwent a 0.3–300 GeV IDV incorporating a flux increase by more than 78% within the first half of 2018 February 9 (MJD 58158; see Table 5).

In Period 3, the source was detected mainly above the 0.3–300 GeV brightness level of $10^{-7}\text{ph cm}^{-2}\text{s}^{-1}$, by showing one symmetric and three two-peak flares (Figure 2D). Moreover, one observed four and three short-term flares with positive and negative asymmetries, respectively (Table 3). Meanwhile, two fast, strong VHE flares were detected with FACT (around MJD 56228 and 562741, respectively). The second instance occurred at the onset of the strongest LAT-band flare, while Mrk 421 was exhibiting only a minor 0.3–10 keV one. On the other hand, the source was detected only 1–2 times with 3σ significance by FACT during the two strongest XRT flares (centered on MJD 56639 and 56702, respectively; the consecutive, negatively-asymmetric LAT-band flares were presented meanwhile). Strong UV activity was observed during the short-term LAT and XRT band flares. However, the source did not exhibit strong X-ray flares in the MAXI and BAT bands. Similar to the above discussed periods, (i) the optical and radio variabilities were even less well-correlated with the LAT-band flares; (ii) the detected eleven flux doubling/halving instances were associated with the aforementioned LAT band flares. However, no 0.3–300 GeV IDVs occurred in that period.

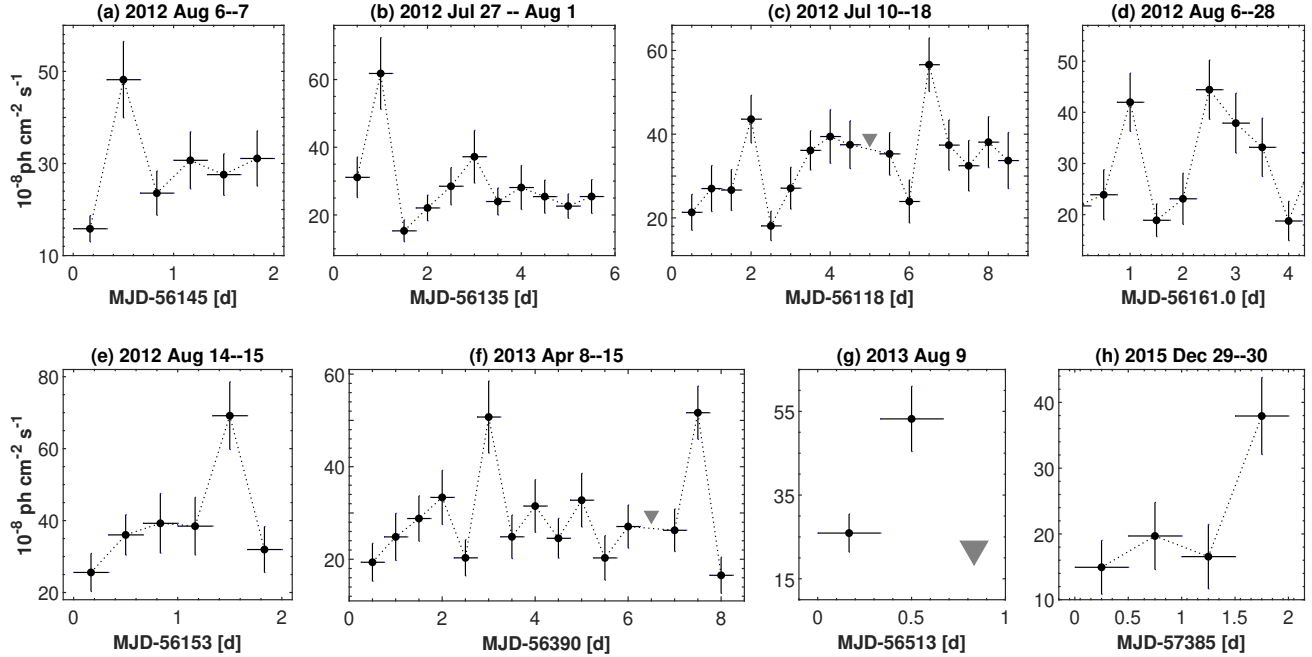


Fig. 4 Selected 0.3–300 GeV IDVs. The downward gray triangles correspond to the upper limits to the LAT-band flux when $TS < 9$ and/or $N_{\text{pred}} < 8$.

A strong MEV–GeV band flux variability was recorded also in the subsequent period, including two symmetric, four two-peak, eight positively and three negatively asymmetric flares (Figure 2E). These instances were superimposed on the gradually declining baseline 0.3–300 GeV brightness level, and this trend was observed during almost 2 years. Note also that the source showed frequent detections with FACT, incorporating seven strong VHE flares. The first, strongest instance coincided with those recorded with LAT, BAT and MAXI (no contemporaneous Swift observations were carried out). Note that the source was not detected with FACT in the epoch of the highest XRT and MAXI-band peak. On the contrary, the strong VHE flare around MJD 57506 was not accompanied by the corresponding 0.3–10 keV activity. However, nearly simultaneous strong flares were observed with LAT, FACT, XRT and BAT. Note also that UV-band peaks had no comparable “counterparts” in the higher-energy bands, except for the flare occurring around MJD 57390. In the latter case, the strongest long-term V-band flare also showed a peak. The source showed 23 instances of the 0.3–300 GeV flux doubling/halving with $\tau_{\text{d,h}} = 2.37\text{--}16.01$ d and $F_{\text{var}} = 24.6(5.8)\text{--}73.2(9.5)$ per cent. The largest-amplitude instance [brightness drop by a factor of ~ 3 during (573)87–90] was preceded by the 0.3–300 GeV IDV incorporating a brightness increase by $\sim 80\%$ within 1 d (Tables 4 and Figure 4h). The second

IDV from this period was characterized by a similar amplitude but showed an opposite cadence (see Table 5).

Finally, Period 6 was also notable for the target’s enhanced MeV–GeV activity: a general elevated base state, lasting almost 14 months, was superimposed by three symmetric, four two-peak, three positively and eight negatively asymmetric flares (Figure 2F). Five strong X-ray flares were recorded with the XRT, and each one was accompanied by the 0.3–300 GeV “counterparts”. However, X-ray flaring activity was relatively moderate in the MAXI-band, and only four detection at the 5σ confidence level was recorded with BAT. The first, second and third XRT-band flares were accompanied by those in the optical–UV bands, followed by a long-term declining trend until the period’s end, and no remarkable activity was observed along with the last two X-ray flares. The first short-term LAT-band flare was accompanied by the highest 43 GHz state of the source. Among 18 instances of the LAT-band flux doubling/halving with $\tau_{\text{d,h}} = 1.06\text{--}12.96$ d, the first one incorporated a 0.3–300 GeV IDV with a factor of > 2 boost in the MeV–GeV brightness within the second half of MJD 59714 (see Tables 4 and 5). Another extreme IDV (brightening by $\sim 80\%$ within 16 hr on MJD 59913) was followed by a flux halving instance with $\tau_{\text{h}} = 1.50$ d. The third IDV (brightening by more than 55% on MJD 59861) was a part of the short-term flare with a negative asymmetry (see Table 3). Note that this period was characterized by the highest-amplitude flux doubling/halving instance dur-

Table 5 Summary of the 0.3–300 GeV IDVs. The initial and final 0.3–300 GeV flux values (Cols 3 and 4, respectively) are given in units of $10^{-8} \text{ph cm}^{-2} \text{s}^{-1}$; Col. (4) presents the reduced Chi-squared and the corresponding degrees-of-freedom; Col. 5: fractional rms variability amplitude (in percents).

Date/MJD (1)	F_i (2)	F_f (3)	χ_r^2/DOF (4)	F_{var} (5)
2012 Jul 11/(56119.)25–50	18.81(3.73)	44.37(6.72)	11.06/1	54.6(12.4)
2012 Jul 11–12/(561)19.5–20.5	44.22(5.85)	14.11(3.05)	15.53/1	74.1(10.8)
2012 Jul 15–16/(561)23.5–24.5	23.92(5.17)	56.60(6.72)	14.86/1	55.4(10.7)
2012 Jul 16/56124	23.92(5.15)	56.60(6.50)	11.52/1	47.9(10.7)
2012 Jul 27/(56135.)0–5	31.11(5.69)	61.79(11.8)	10.89/1	84.7(16.3)
2012 Jul 27–28/(561)35.5–36.5	61.79(11.8)	14.49(3.16)	14.99/1	84.7(16.3)
2012 Aug 6/(56145.)33–67	15.83(2.80)	48.20(8.29)	13.66/1	68.8(13.9)
2012 Aug 6/(56)145.67–166.00	48.20(8.29)	23.83(4.66)	10.95/1	36.7(10.5)
2012 Aug 15/(561)54.67–55.0	68.66(9.5)	26.26(5.55)	14.85/1	61.0(11.8)
2012 Aug 22–23/(561)61.5–62.5	42.45(6.07)	14.68(3.20)	16.38/1	66.6(12.2)
2012 Aug 23–24/(561)62.5–63.5	22.10(5.01)	45.92(5.84)	10.85/1	49.5(11.5)
2012 Aug 28–29/(561)67.67–68.33	48.30(9.09)	16.21(3.26)	11.03/1	67.1(15.3)
2013 Mar 26/(56377.)00–50	58.95(9.72)	23.63(9.80)	10.99/1	59.1(1.35)
2013 Apr 10/56392	20.28(3.91)	50.73(7.76)	13.46/1	58.1(1.30)
2013 Apr 10–11/(56)392.5–393.5	50.73(8.76)	20.30(4.19)	10.93/1	45.2(11.8)
2013 Apr 14–15/(56)396.5–397.5	26.26(4.75)	51.66(6.10)	10.96/1	43.9(10.2)
2013 Apr 15/(56397.)417–500	106.38(18.54)	36.61(7.79)	12.04/1	66.1(14.4)
2013 Aug 9/(56513.)00–50	24.92(4.30)	54.20(7.79)	10.85/1	49.9(11.5)
2015 Dec 30/57386	15.05(3.51)	39.93(6.65)	10.91/1	61.0(14.0)
2016 May 18/57526	12.03(2.82)	31.34(4.8)	12.03/1	60.3(13.1)
2018 Feb 9/(58158.)0–5	26.19(4.82)	66.49(11.12)	11.04/1	57.9(13.4)
2022 May 8/59707.5–59708.0	24.12(5.54)	4.85(0.96)	11.75/1	90.0(19.8)
2022 May 15/59714.5–59715.0	15.65(3.75)	55.74(11.43)	10.99/1	75.7(17.4)
2022 Oct 9/59861	24.45(3.71)	55.74(11.43)	10.89/1	54.9(12.6)
2022 Nov 30/59913.33–59914.00	14.08(4.14)	38.31(6.03)	10.97/1	62.4(14.3)

ing 2008–2023 [$F_{\text{var}} = 95.8 \pm 18.7$ per cent, factor of ~ 5 drop during MJD (5994)3–6].

4 Spectral Results

The distribution of the Γ -values obtained from the power-law spectral analysis for the entire 2008–2023 period is presented in Figures 5A1–5A6, each histogram representing the results obtained from the different time integration from two weeks down to one day. The distribution details (maximum, minimum, mean and peak values) are provided in Table 6. The latter demonstrates that the source showed a very large spectral variability from the extremely hard Γ -values ($\Gamma \lesssim 1.5$) to extremely soft ($\Gamma \gtrsim 2.5$) spectra. Namely, the overall range of the photon index $\Delta\Gamma = 0.99(0.20)$ for the two-weekly binned LAT data and $\Delta\Gamma = 1.65(0.31)$ in the case of the 1–3 day integrations. The distribution peaks are derived by fitting the corresponding histogram with the lognormal function, which generally

showed slightly better statistics compared to other (e.g., Gaussian) functions (see Table 7).

The peak and mean values from the histograms, corresponding to the different time integrations during the entire 2008–2023 period, are close to each other ($\Gamma_p = 1.75(0.01)–1.79(0.01)$, $\Gamma_{\text{mean}} = 1.79(0.01)–1.82(0.01)$). Note that the Γ -values from the time bins corresponding to the non-robust detections of the source are not included in the distribution study. Since the percentage of such bins are gradually higher with shorter integration times, the distribution from the latter are biased towards the higher MeV–GeV states of Mrk 421, and the slight differences between the Γ_p and $\bar{\Gamma}$ values could be primarily due to this selection effect. The distributions of the photon index from the aforementioned six periods are relatively more different (see the bottom part of Table 6 and Figures 6a–6f): the ranges of the peak and mean values are $\Gamma_p = 1.73(0.01)–1.82(0.01)$ and $\Gamma_{\text{mean}} = 1.75(0.01)–1.84(0.01)$, respectively. On average, the 0.3–300 GeV spectra showed the hardest distribution peak in Period 1 which was

Table 6 Distribution of the photon indices from the power-law and logparabolic 0.3–300 GeV spectra, corresponding to the different time integrations (from two weeks down to 1 d) during 2008–2023 and periods (bottom, only for the Γ -index). The maximum, minimum, mean and distribution peak values are presented in the first, second, 3rd and 4th rows for the both parts of the table, respectively.

2008–2023									
	$\Gamma(2\text{ w})$	$\Gamma(1\text{ w})$	$\Gamma(4\text{ d})$	$\Gamma(3\text{ d})$	$\Gamma(2\text{ d})$	$\Gamma(1\text{ d})$	$\alpha(2\text{ w})$	$\alpha(1\text{ w})$	$\alpha(4\text{ d})$
Max.	2.55(0.18)	2.59(0.26)	2.83(0.38)	2.89(0.28)	2.90(0.30)	2.86(0.28)	1.98(0.07)	2.44(0.20)	2.62(0.20)
Min.	1.56(0.09)	1.37(0.15)	1.31(0.09)	1.24(0.13)	1.24(0.12)	1.21(0.13)	1.18(0.07)	1.13(0.10)	1.05(0.13)
Mean	1.80(0.01)	1.80(0.01)	1.80(0.01)	1.79(0.01)	1.82(0.01)	1.82(0.01)	1.57(0.02)	1.63(0.01)	1.58(0.01)
Peak	1.79(0.01)	1.76(0.01)	1.77(0.01)	1.76(0.01)	1.76(0.01)	1.75(0.01)	1.55(0.02)	1.52(0.01)	1.50(0.01)
2008–2023									
	Γ								
	$\alpha(3\text{ d})$	$\alpha(2\text{ d})$	$\alpha(1\text{ d})$	Per 1	Per 2	Per 3	Per 4	Per 5	Per 6
Max.	2.39(0.20)	2.61(0.25)	2.60(0.23)	2.31(0.19)	2.38(0.22)	2.48(0.25)	2.71(0.25)	2.64(0.29)	2.34(0.23)
Min.	1.05(0.13)	1.10(0.14)	1.03(0.17)	1.51(0.07)	1.41(0.07)	1.30(0.11)	1.24(0.11)	1.30(0.14)	1.29(0.13)
Mean	1.61(0.01)	1.56(0.01)	1.73(0.01)	1.82(0.01)	1.75(0.01)	1.82(0.01)	1.76(0.01)	1.84(0.01)	1.83(0.01)
Peak	1.50(0.01)	1.51(0.01)	1.57(0.01)	1.76(0.01)	1.74(0.01)	1.77(0.01)	1.78(0.01)	1.82(0.01)	1.78(0.01)

characterized by one the strongest flaring activity of the source (see Section 3.1).

As noted above, the LAT-band power-law spectra of Mrk 421 were sometimes extremely hard with $\Gamma \lesssim 1.5$, and this happened within the different time intervals ranging from intraday to 25 days (see Table 8). Note that each period contained a different number of extremely hard 0.3–300 GeV spectra (see Table 8 and Section 5.3 for the corresponding physical implications). Moreover, we checked the 4-weekly binned LAT data for possible hardening beyond 10 GeV (see Section 5.3 for the discussion in the context of hadronic cascades). This integration time was required to achieve the target’s robust detection in the 10–300 GeV energy range for the most of the time bins. Table 9 presents 23 cases of spectral hardening beyond 10 GeV with $\Gamma = 0.93 \pm 0.20$ to $\Gamma = 1.65 \pm 0.16$.

The parameter Γ showed a strong variability on various timescales, as shown in Figure 1 where the timing behaviour of the photon index is presented by different time integrations (similar to the 0.3–300 GeV photon flux). First of all, these instances were related to the emergence of the extremely hard spectra. The most extreme spectral hardening/softening instances (the largest and/or fastest) are presented in Table 8. The largest-amplitude hardening by $\Delta\Gamma = 1.34(0.12)$ occurred during MJD (562)24–26 (Period 5, in the epoch of one of the strongest LAT-band flaring activity), and the instance with the comparable amplitude (although occurring within 16 d) was observed after the largest softening by $\Delta\Gamma = 1.60(0.33)$ within 18 d [MJD (59)385–402]. Note that hardenings/softenings by $\Delta\Gamma > 1$ (taking into account the error ranges) during 2–5 days was observed more than 10 times. For example, the spectrum showed a subsequent softening and harden-

ing by $\Delta\Gamma = 1.30(0.28)$ and $\Delta\Gamma = 1.12(0.29)$, respectively, within the 5-d time interval [(561)08–12, in Period 5].

As noted above, only a minority of the 0.3–300 GeV spectra (5% to 13% with the different time integrations) showed a spectral curvature with the significance 2σ and higher. Namely, the lowest percentage is associated with the 2-day binned data, while the highest one – with the 4 d integrations. Note that the reference energy E_0 was generally close to 1.286 GeV when leaving this parameter free during the spectral fit fit the logparabolic model and, consequently, we re-fitted the curved spectra by fixing E_0 to this value (in order to minimize the uncertainties related to the photon index α and curvature parameter β). The distribution of the α -values from the different time integrations during the entire 2008–2023 period is presented in Figures 5B1–5B6, and the corresponding distribution properties are provided in Table 6. As far as we see, the photon-index range is relatively narrow ($\Delta\alpha = 0.80(0.10)$) in the case of 2-weekly binned data, and it increases to $\Delta\alpha = 1.57(0.24)$ in the case of the 4-d integration. Similar to the Γ -index, the corresponding histograms are relatively well-fitted with the lognormal model (except for the two-week integration; see also Table 6), and the α -values were sometimes extremely hard down to $\alpha = 1.03 \pm 0.13$. Note that the logparabolic LAT-band spectra showed a concentration within some time intervals. Finally, the curvature parameter showed a range between $\beta = 0.12 \pm 0.06$ (two-weekly binned data from the flaring epochs) to $\beta = 1.64 \pm 0.22$ (1-d time integration).

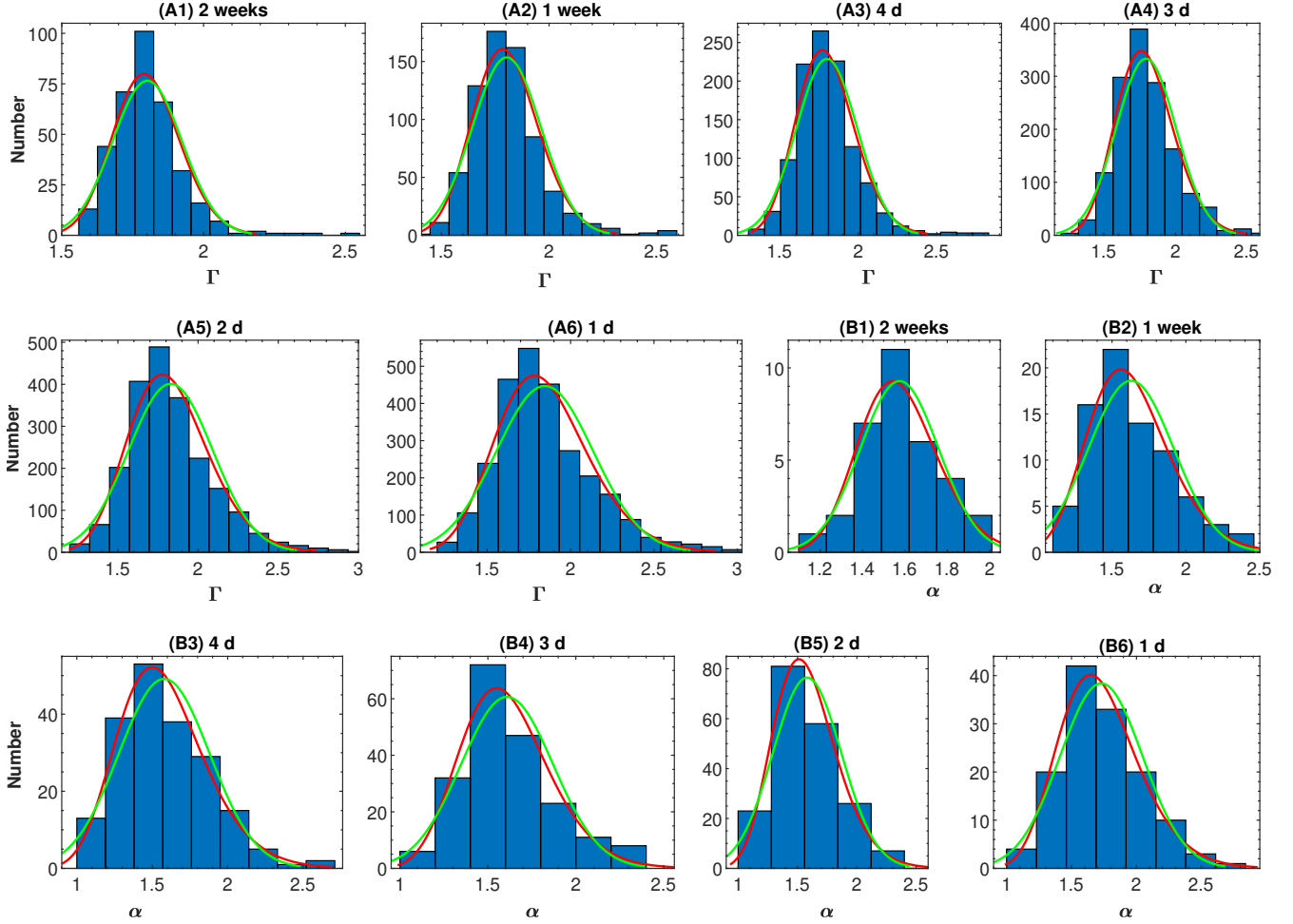


Fig. 5 Distribution of the photon indices from the power-law and logparabolic spectra during 2008–2023, derived from the 0.3–300 GeV data by using different time integrations. The red and green curves show the lognormal and Gaussian fits to the histograms, respectively.

5 DISCUSSION AND CONCLUSIONS

5.1 Variability Character

Intense studies of the MWL flux variability pattern provide us with one of the most efficient tools for drawing conclusions about the unstable processes occurring in blazars. Especially important objective is related to the detection of the periodic flux variability, which can be associated with the jet precession (see, e.g., Tavani et al. 2008; Sobachi et al. 2017). Namely, there should be a primary BH with a jet pointed to the observer and accretion disc, while the secondary, smaller-mass BH is moving on a highly eccentric orbit around the system’s mass center. The dominant effect is simply an imprint of the primary BH’s orbital velocity on the jet, causing the jet’s viewing angle to vary by the greatest amount, and the highly-relativistic ejected material is expected to have the same velocity component in the observer’s rest frame. Consequently, the jet will

precess with respect to the distant observer, and one should observe a periodic flux variability.

Generally, the clear identification of periodic variability of blazar is problematic owing to the complexity of light curves and the lack of data trains large enough to provide an adequate sampling over large time intervals. The long-term regular LAT observations are especially valuable in this regard. In order to detect a possible periodical behavior of Mrk 421 from these observations, we constructed the Lomb-Scargle (LSP) periodogram (Lomb 1976; Scargle 1982), representing an improved Fourier-based technique which is designed for unevenly-sampled time series g_n without interpolation for the data gaps (VanderPlas 2018):

$$P(f) = \frac{A^2}{2} \left(\sum_n g_n \cos(2\pi f[t_n - \tau]) \right)^2 + \frac{B^2}{2} \left(\sum_n g_n \sin(2\pi f[t_n - \tau]) \right)^2, \quad (4)$$

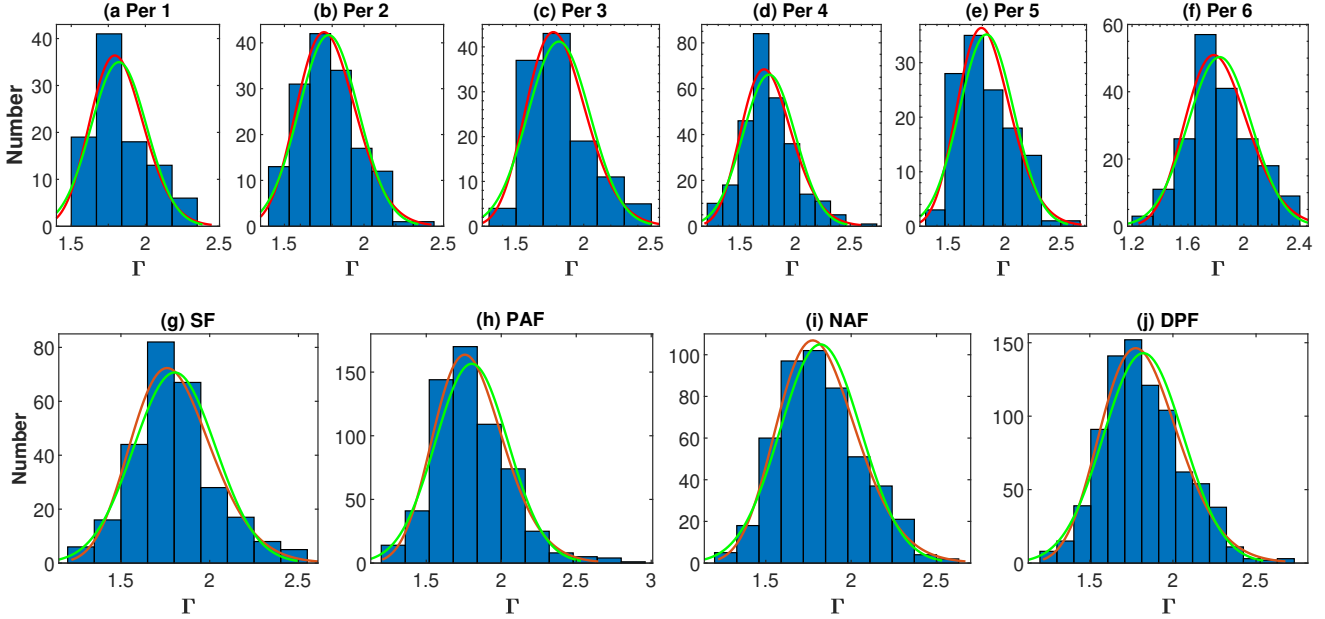


Fig. 6 Distribution of the photon-index Γ in different periods [panels (a)–(f)], as well as for those time intervals showing the LAT-band flares of Mrk 421 with different profiles [panels (g)–(j)]; SF – symmetric flares, PAF – positively-asymmetric flares, NAF – negatively-asymmetric flares and DPF – double-peak flares]. The red and green curves show the lognormal and Gaussian fits to the histograms, respectively.

where A , B , and τ are the arbitrary functions of the frequency f and observing times $\{t_i\}$. The LSP exhibits the most significant spectral power peak in the case of the periodicity existence, and estimates its significance by testing the false alarm probability of the null hypothesis.

Since every periodicity searching technique requires at least one alternative check, we adopted the weighted wavelet Z-transform (WWZ) method (Foster 1996 and references therein), which performs a periodicity analysis in both the time and frequency domains. It is defined as follows

$$WWZ = \frac{(N_{\text{eff}} - 3)V_y}{2(V_x - V_y)}, \quad (5)$$

with N_{eff} , the so-called effective number of data points; V_x and V_y , the weighted variation of the data $x(t)$ and model function $y(t)$, respectively. The WWZ is based on the Morlet wavelet (Grossmann & Morlet 1984) $f(z) = e^{-cz^2}(e^{iz} - e^{-1/4c})$, where the constant $e^{-1/4c}$ is selected in the manner the wavelet’s mean value to be zero. Similar to the LSP, the WWZ technique is robust against missing data.

Figure 7 presents the WWZ and LSP plots of corresponding to the LAT-band light curves of Mrk 421 from the 2008–2023 period, constructed on the basis of different time integrations. In the WWZ plot, the possible period should emerge as a permanent narrow horizontal peak, corresponding to the most significant peak in

the LSP plot (see, e.g., O’Neil et al. 2022; VanderPlas 2018). The latter also contains the curves corresponding to the detection significances with 2σ and 3σ , determined by using the recipe of Emmanoulopoulos et al. (2013). However, no highly significant periodical variability was found, since only the peaks with a significance of 3σ and higher correspond to genuine periodicity (O’Neil et al. 2022). The significances of the existing PSD peaks, corresponding to some bright strips in the WWZ plots, do not reach the 3σ significance. The bright LSP stripe around $P=1000$ d in Figure 7, changing in width with time and shifting to larger values after about MJD 56500, can be explained as a red noise leak (see O’Neil et al. 2022).

As for the past studies, (Bhatta 2019; Bhatta & Dhital 2020) claimed a periodicity detection for Mrk 421 from the Fermi-LAT data. In addition to the issues related to the analysis of the LAT data (e.g., the energy range of 0.1–300 GeV instead of 0.3–300 GeV generally adopted for HBLs; see Section 2.1), the reported periods (285 and 330 days) were detected below the 3σ significance and/or showed some changes with time, as inherent to the red noise leak (similar to our result). Nevertheless, this detection was not confirmed by Tarnopolski et al. (2020) from the same 10-yr data by adopting some additional methods of the periodicity check.

The longer-term enhanced activity (e.g., those exhibited by Mrk 421 in the LAT-band) could be result from the propagation and evolution of relativistic shocks through the observer-pointed jet (see, e.g.,

Table 7 Goodness-of-fit for the flux and photon-index distributions in various energy bands. The distribution fits are performed by using the Gaussian and lognormal functions (Columns 2 and 3, respectively). The acronyms SF, PAF, NAF and DPF have the same meanings as in Figure 6.

Energy Band	$\chi^2_r/\text{DOF}(\text{Gauss})$	$\chi^2_r/\text{DOF}(\text{Logn})$
(1)	(2)	(3)
Γ (2 w)	1.13/14	0.99/14
α (2 w)	1.06/6	0.94/6
Γ (1 w)	1.14/14	1.03/12
α (1 w)	1.29/8	1.07/8
Γ (4 d)	1.16/14	1.06/14
α (4 d)	1.27/8	1.02/8
Γ (3 d)	1.15/11	1.05/11
α (3 d)	1.22/6	1.08/6
Γ (2 d)	1.19/13	1.08/13
α (2 d)	1.27/6	1.16/6
Γ (1 d)	1.29/15	1.10/15
α (1 d)	1.24/7	1.06/7
Γ (2 d, Per 1)	1.21/4	1.10/4
Γ (2 d, Per 2)	1.20/7	1.09/7
Γ (2 d, Per 3)	1.12/5	0.96/5
Γ (2 d, Per 4)	1.22/10	0.97/10
Γ (2 d, Per 5)	1.22/7	1.15/7
Γ (2 d, Per 6)	1.20/7	1.10/7
Γ (2 d, SF)	1.21/10	1.12/10
Γ (2 d, PAF)	1.18/13	1.04/13
Γ (2 d, NAF)	1.22/12	1.14/12
Γ (2 d, DPF)	1.24/16	1.07/16
$F_{0.3-300 \text{ GeV}}$ (2 w)	1.39/10	0.98/10
$F_{0.3-300 \text{ GeV}}$ (1 w)	1.43/10	1.02/10
$F_{0.3-300 \text{ GeV}}$ (4 d)	1.55/13	1.07/13
$F_{0.3-300 \text{ GeV}}$ (3 d)	1.55/14	1.09/14
$F_{0.3-300 \text{ GeV}}$ (2 d)	1.88/14	1.06/14
$F_{0.3-300 \text{ GeV}}$ (1 d)	1.71/13	0.95/13
$F_{0.3-300 \text{ GeV}}$ (2 d, Per 1)	2.36/9	1.11/9
$F_{0.3-300 \text{ GeV}}$ (2 d, Per 2)	1.45/6	0.96/6
$F_{0.3-300 \text{ GeV}}$ (2 d, Per 3)	1.39/10	0.98/10
$F_{0.3-300 \text{ GeV}}$ (2 d, Per 4)	1.36/9	1.13/9
$F_{0.3-300 \text{ GeV}}$ (2 d, Per 5)	1.35/9	1.12/9
$F_{0.3-300 \text{ GeV}}$ (2 d, Per 6)	1.66/7	1.16/7
$F_{0.3-300 \text{ GeV}}$ (2 d, SF)	1.48/10	0.97/10
$F_{0.3-300 \text{ GeV}}$ (2 d, PAF)	1.54/11	1.10/11
$F_{0.3-300 \text{ GeV}}$ (2 d, NAF)	1.37/10	1.15/11
$F_{0.3-300 \text{ GeV}}$ (2 d, DPF)	1.33/10	1.01/16

Böttcher & Baring 2019). In turn, a shock can be triggered by the instabilities occurring in the innermost accretion disk, which momentarily saturate the jet with the highly-energetic plasma carrying much larger pressure than the relatively steady jet plasma downstream (Sokolov et al. 2004 and references therein). This phenomenon could be reflected in a lognormal flaring activity of the source on various timescales, since the latter may indicate a variability imprint of the accretion disk onto the jet (see, e.g., Rieger 2019). Namely, independent density fluctuations can emerge in the disk on the local viscous timescales, characterized by a negligible damping. These instances can propagate in the direction of the innermost disc area, merge there and

produce a multiplicative behavior. The combined fluctuation can be transferred into the jet flow (e.g., as an abrupt enhancement in the jet collimation rate), and the jet emission (including the LAT-band one) can be modulated correspondingly. Consequently, a lognormal variability in the different energy range and over various timescales is then anticipated (Giebels & Degrange 2009; Rieger 2019).

The emission from the proton-induced synchrotron cascades (Mannheim 1993 and references therein), or that from the magnetospheric IC pair production processes (Levinson & Rieger 2011) are also thought to yield log-normal flux distributions. However, there can be some limitations by the gap travel time for the magnetospheric processes and from the dynamical or escape properties of the hadronic cascades (Rieger 2019). Furthermore, lognormal variability can be produced by random fluctuations in the particle acceleration rate (Sinha et al. 2018). In that case, fluctuations in the acceleration rate can be also characterized by the Gaussian distribution of the photon-index along with the lognormal flux distribution.

We checked the LAT-band light curves of Mrk 421 constructed with different time integrations for the presence of lognormal variability. Figures 8a–8d and Table 7 demonstrate that a lognormality was inherent to the target during the entire period of our study: the lognormal function fits significantly better with the histograms constructed by using the integrations from two weeks down to one day than the Gaussian one. A similar situation was also for the samples containing the 0.3–300 GeV flux values from Periods 1–6, characterized by the different levels of LAT-band flaring activity of the target (Figures 8e–8h). As noted in Section 4, the distribution of the Γ -values sometimes was not very different from a Gaussian shape. Note that the lognormal flux variability along with a Gaussian distribution of the photon index can stem from the random fluctuations in the particle acceleration rate (see above). Note that a gradual (relatively slow) acceleration of the particles responsible for the IC upscattering of low-energy photons to the MeV–GeV range could be produced by stochastic (second-order) Fermi mechanism operating in the jet region with low magnetic field and high matter density (Virtanen & Vainio 2005). On the contrary, rapid injection of very energetic particles is inherent with the first-order Fermi mechanism within the Bohm’s limit of particle diffusion (Virtanen & Vainio 2005). We suggest that there could be frequent random transitions from dominance of the first-order Fermi process into that of stochastic acceleration and vice versa during the aforementioned periods. Note that the dominance of the Fermi-I process (operating in Bohm’s limit) is reflected in the clockwise (CW) spectral evolution of the

Table 8 Extremely hard power-law spectra (extract). For each photon index value, the corresponding time range in MJD and UTC, N_{pred} and TS values are presented.

Dates/MJDs	N_{pred}	TS	Γ	Dates/MJDs	N_{pred}	TS	Γ
2008 Aug 19–20/(546)98–99	10	81	1.39(0.12)	2010 Oct 30–31/(55)499–500	14	115	1.48(0.10)
2008 Aug 25–29/(5470)4–5	44	235	1.37(0.08)	2010 Nov 29–30/55529	9	62	1.28(0.13)
2008 Sep 22–23/(5473)1–2	11	95	1.24(0.11)	2011 Jan 8–9/(555)69–70	19	162	1.31(0.09)
2008 Sep 28–29/(5473)7–8	9	80	1.28(0.11)	2011 Feb 8–15/(5560)0–7	56	310	1.53(0.05)

flare in the flux–photon index plane (Tammy & Duffy 2009). On the contrary, the source follows a counter-clockwise (CCW) spectral evolution when the Fermi-II process is dominant (Tramacere et al. 2009). Note that the CW-to-CCW or converse transitions during single X-ray flares in Mrk 421 in those periods were reported by Kapanadze et al. (2018b). Similar situations were evident also during other periods (see Kapanadze et al. 2016, 2017a, 2018a, 2020, 2024, detecting also the X-ray and FACT-band lognormality in the target).

Note that the source sometimes showed symmetric short-term flares accompanied by very hard photon indices within some time bins, which could be powered by ”blobs” of magnetized, nonthermal plasma. In turn, such blobs can be produced by the RMR operating in the jet and not related to the AD instabilities (see below). The flux variability in the corresponding time intervals is not expected to show a lognormality and produce outliers from the histograms (as presented in Figure 8), along with those flux values containing the contribution from other local, purely jet-inherent processes. Namely, each histogram shows outliers or even low-amplitude secondary peaks at the fluxes higher than $\sim 1.5 \times 10^{-7} \text{ph cm}^{-2} \text{s}^{-1}$. Moreover, the presence of those acceleration processes other than those involving random fluctuations in the particle acceleration rate is reflected in deviations of the photon-index distributions from the Gaussian shape, as demonstrated by each histogram presented in Figures 5–6.

As shown in Section 3.1, short-term LAT-band flares were frequently seen in the epochs of the X-ray flaring activity, hinting at the connection between these instances, e.g., via the IC-upscatter of the X-ray photons in the Klein-Nishina (KN) regime. The later is notable for the suppression of the γ -ray emission and, consequently, the fractional variability amplitude was generally at least 50% lower than that observed with XRT in the 0.3–10 keV energy range (see Table 2). Note that Table 11 presents the time intervals of the 4-week duration when the LAT observations showed a softening at the energies beyond 1 GeV or 10 GeV compared to the lower-energy LAT-band part of the spectrum. These instances should be related to the IC-upscatter of X-ray photons to the GeV energies in the KN-regime (versus the upscatter of lower-energy

photons in the Thomson regime to the energies below 1 GeV or 10 GeV). Consequently, the light curves constructed for the separate 0.3–1 GeV, 1–10 GeV and 10–300 GeV bands do not follow each other closely in the corresponding time intervals (Figure 9). Moreover, the possible KN-suppression weakened the expected strong correlation between the fluxes extracted from these bands down to $\rho=0.63(0.07)$ – $0.73(0.06)$: the data points corresponding to the instances provided in Table 11 produce outliers from the scatter plots $F_{0.3-1\text{GeV}} - F_{1-10\text{GeV}}$, $F_{0.3-1\text{GeV}} - F_{10-300\text{GeV}}$ and $F_{1-10\text{GeV}} - F_{10-300\text{GeV}}$ (see the bottom row of Figure 9).

A similar situation was also found with the MAXI-band variability in Periods 2–4, hinting at the significant portion of the hard X-ray emission among the ”seed” photons for the upscattering to the MeV–GeV energies in the KN-regime. Note also that the F_{var} values for the 1–10 GeV and 10–300 GeV bands from the intervals presented in Table 11 are lower than their ”counterpart” in the 0.3–10 GeV band, while the source generally showed a trend of higher F_{var} with increasing energy: $F_{\text{var}}=34.4(1.10)$ in the 0.3–10 GeV band versus $F_{\text{var}}=50.1(1.1)\%$ beyond 10 GeV for the entire set of the 4-weekly bins.

The exception was Period 1 where the LAT-band F_{var} value was higher than its 0.3–10 keV counterpart. However, no XRT observations were carried out in the epoch of the strongest 0.3–300 GeV flaring activity (as discussed in Section 3.1.1) and, consequently, no firm conclusion can be drawn. However, a similar situation (significantly lower fractional amplitude) was in the case of the regular MAXI observations: the 5σ -detections of Mrk 421 were not frequent and occurred mostly during the long-term LAT-band outburst, but the hard X-ray flaring activity was considerably weaker and the peak states were recorded only during the LAT-band decline epoch. Moreover, the regular BAT observations yielded only two 5σ -detections of the target in the epoch of the LAT-band outburst, showing relatively low 15–150 KeV states. A significantly stronger BAT-band activity with more frequent 5σ -detections and much higher hard X-ray fluxes were recorded in other periods (except for Period 1; see the corresponding panels in Figure 2). Similarly, higher MAXI-band states occurred in Periods 2, 6, 4, 8 and 10–11. Note

Table 9 List of the harder 10–300 GeV spectra along with the corresponding MJD interval, N_{pr} and TS values.

Dates/MJDs (1)	0.3–1 GeV			1–10 GeV			10–300 GeV		
	N_{pred} (2)	TS (3)	Γ (4)	N_{pred} (5)	TS (6)	Γ (7)	N_{pred} (8)	TS (9)	Γ (10)
2008 Aug 5—Sep 1/(56)683–710	108	193	1.57(0.15)	86	577	1.66(0.09)	14	198	1.37(0.12)
2008 Sep 30—Oct 27/(567)39–66	81	133	1.91(0.23)	62	319	2.11(0.19)	12	143	1.50(0.12)
2009 Apr 14—May 11/(569)35–62	85	161	1.89(0.20)	63	352	1.94(0.16)	16	240	1.61(0.10)
2009 Jun 9—Jul 7/54991–55018	114	233	2.16(0.18)	82	558	1.99(0.15)	13	152	1.72(0.12)
2009 Aug 4—31/(550)47–74	100	240	1.53(0.14)	48	303	1.85(0.17)	11	126	1.54(0.12)
2010 May 11—Jun 7/(553)27–54	100	196	2.14(0.18)	69	463	1.62(0.13)	13	197	1.42(0.11)
2013 Sep 24—Oct 21/(565)56–83	114	235	1.72(0.18)	79	544	1.64(0.12)	16	193	1.37(0.12)
2014 Jan 14–Feb 10/(566)71–88	146	285	1.83(0.16)	102	589	2.05(0.14)	15	194	1.69(0.11)
2014 Nov 18—Dec 15/56979–57006	122	348	1.73(0.14)	92	713	1.68(0.09)	28	388	1.57(0.08)
2016 Sep 20—Oct 17/(576)51–78	42	63	1.95(0.26)	13	35	2.72(0.38)	8	73	1.65(0.16)
2018 Jun 26—Jul 23/(58)295–322	46	74	2.79(0.36)	25	131	1.90(0.22)	9	121	1.47(0.13)
2018 Oct 16—Nov 12/(584)07–34	88	165	1.77(0.20)	70	439	1.87(0.17)	10	140	1.34(0.14)
2018 Dec 11—2019 Jan 7/(584)63–90	111	194	2.18(0.19)	56	256	2.17(0.20)	17	242	1.81(0.11)
2019 Apr 2—29/(58)575–602	102	165	2.92(0.37)	94	606	1.71(0.11)	16	264	0.97(0.20)
2019 Apr 30—May 27(586)03–30	62	100	1.91(0.25)	40	178	2.06(0.22)	15	253	0.93(0.20)
2019 May 28—Jun 24/(586)31–58)	116	220	1.74(0.17)	54	311	1.69(0.16)	10	124	1.31(0.14)
2019 Aug 20—Sep 16/(587)15–42	39	73	2.62(0.36)	59	353	1.94(0.16)	8	98	1.18(0.18)
2019 Nov 12—Dec 8/(58)799–826	142	327	1.30(0.20)	91	553	1.91(0.18)	16	202	1.29(0.12)
2020 Aug 18—Sep 14/(59)079–106	60	124	1.83(0.24)	33	220	1.70(0.18)	8	107	1.41(0.14)
2021 Sep 14—Oct 11/(594)71–98	92	185	1.51(0.17)	42	215	1.98(0.18)	12	130	1.50(0.12)
2022 Nov 8—Dec 5/(59)891–918	163	332	1.94(0.15)	130	839	1.87(0.11)	24	304	1.47(0.10)
2022 Dec 6—2023 Jan 2/(599)19–46	152	372	1.83(0.14)	93	674	1.81(0.13)	22	305	1.44(0.10)
2023 Jan 31—Feb 27/59975–60002	97	237	1.60(0.15)	81	541	1.82(0.15)	10	155	1.55(0.11)

that the strongest LAT-band outburst in 2012 coincided with onset of the strong, long-term V-band flare. We suggest that the latter was probably triggered by the long-term, strong increase in the collimation rate of leptons capable of producing a strong optical flare (but not an X-ray one). Consequently, an IC-upscatter of these lower-energy photons to MeV–GeV energies in the Thomson regime yielded a long-term boost in the LAT-band emission, which was not suffered of the KN-suppression due to the lack of corresponding ultrarelativistic electron population.

Moreover, the MAXI-band fractional amplitude was lower compared to the 0.3–300 GeV counterpart also during Periods 3–4 and 6, whereas a similar situation was observed also in the BAT band or the source did not show variability at the 3σ confidence level. The difference was especially large in Period 7: the MAXI-band F_{var} quantity was by a factor 2 lower than that derived from the LAT observations, and the flux variabilities recorded in these bands were obviously not correlated. Consequently, an IC-upscatter of hard X-ray photons to the MeV–GeV energies in the KN-regime practically could not occur in that period.

Note also that the fluxes, corresponding to the highest LAT-band states in Periods 1 and 3–5 produce outliers from the lognormal distribution. These states generally were recorded during the relatively fast flares superimposed on the long-term one. We suggest that these instances could be triggered by the shock interaction with the jet inhomogeneities, the origin of which was related to the jet instabilities (e.g., strong turbulent structures; Marscher 2014). Since such structures have no relation with the AD instabilities, consequently, the associated highest LAT-band fluxes could not follow a lognormal distribution.

Finally, the source showed a lognormal variability during the FACT observations in the different periods (see Kapanadze et al. 2020, 2024). As discussed in Section 3.1, Mrk 421 frequently underwent simultaneous flaring activity in the VHE and 0.3–10 keV energy ranges (and reported from a number of the MWL studies; see Horan et al. 2009; Acciari et al. 2014; Aleksic et al. 2015a,b; Ahnen et al. 2016 etc.) that is in accordance with the one-zone SSC scenario and shows a generation of the corresponding emissions by the same electron population. However, some strong VHE flares in Periods 4–5 were not accompa-

Table 10 Summary of the largest LAT-band hardening/softening instances, shown with arrows preceded with the maximum duration of the given instance (extract).

Dates/MJDs	Photon index (error) /Maximum duration of the hardening/softening instance
2008 Aug 5–15/(546)83–93	1.65(0.11)[6d] → 2.31(0.22)[4d] → 1.33(0.15)[4d] → 2.32(0.22)[3d] → 1.60(0.13)
2008 Aug 19–27/(54)697–705	1.39(0.12)[4d] → 2.26(0.21)[6d] → 1.33(0.13)
2008 Sep 14–30/(547)23–39	2.00(0.15)[10d] → 1.24(0.12)[4d] → 2.20(0.15)[6d] → 1.28(0.12)
2008 Oct 7–22/(547)46–61	1.62(0.13)[8d] → 2.26(0.16)[9d] → 1.54(0.13)

nied by the comparable 0.3–10 keV ”counterparts” (see Section 3). The VHE flux peaked days before the X-ray one during the giant flare in 2004 that was impossible to explain via the standard one-zone SSC model, and Blazewski et al. (2005) suggested this instance to be an ”orphan” TeV flare. Acciari et al. (2011) also found the elevated X-ray states not being accompanied by TeV flaring and conversely in 2006–2008 etc. These instances show that the one-zone SSC models was not always acceptable for the target. For example, a fast strong VHE flare without a significant simultaneous X-ray flaring activity on MJD 57788 was interpreted by Acciari et al. (2021) as follows: the VHE flare was caused by the appearance of a more compact second blob of highly-energetic electrons with considerably narrow energy range that could have been produced by stochastic acceleration, by the RMR, or by electron acceleration in the magnetospheric vacuum gap, close to the central SMBH. Note that the MAGIC energy range is partially overlapped by the 10–300 GeV band used by us for constructing the light curve presented in the 3rd panel of Figure 9. However, the latter is based on the 4-weekly integration and, consequently, the strong one-day VHE flare on MJD 57788 is smoothed out, showing only a low-amplitude peak in that epoch. Note that the one-day binned data from the entire 0.3–300 GeV band show the target’s robust detection and a flaring state corresponding to $(1.7 \pm 0.35) \times 10^{-7} \text{ph cm}^{-2} \text{s}^{-1}$ (not resolvable in the separate 0.3–1 GeV, 1–10 GeV and 10–300 GeV sub-bands).

Note that the selection of these periods was based on relatively enhanced LAT-band flaring activity on timescales of several months to more than 1 yr which, in turn, could be caused by an enhanced matter collimation rate on yearly timescales. This phenomenon could trigger also the baseline 0.3–10 keV flux variability on yearly timescales in our target (see Kapanadze et al. 2024), and it is even more clearly expressed in other nearby X-ray bright, TeV-detected HBLs Mrk 501 and 1ES 1959+650 (Kapanadze et al. 2018c, 2023).

Another experimental confirmation for the shock presence in the jet of Mrk 421 was provided by the 2–8 keV observations with the Imaging X-ray Polarimetry Explorer (IXPE) carried out on 2022 May 4 (Di Gesu et al. 2022): the higher level of the X-ray

linear polarization degree compared to longer wavelengths, and the absence of significant polarization variability was explained as a shock was the most likely X-ray emission site in the jet during that observation.

Our study has revealed 175 instances of 0.3–300 GeV flux doubling/halving with the timescales $\tau_{d,h}$ ranging from 5 hr to ~ 17.5 d and generally associated with short-term flares. These instances were observed in all 6 periods discerned within our study (as well as in the intermediate time intervals), with significantly larger numbers in those periods characterized by the strong LAT-band activity of Mrk 421. These detections allow us to constrain the upper limit to the size of LAT-band emission zone as (Saito et al. 2013 and references therein)

$$R_{\text{em}} \leq c\tau_{d,h}\Gamma_{\text{em}}/(1+z). \quad (6)$$

By assuming that the jet axis is aligned near the line-of-sight with the critical angle, then $\Gamma_{\text{em}} = \delta$ (Balokovic et al. 2016) and we can adopt $\delta = 25$ (the value of the Doppler factor frequently derived for Mrk 421 from the different studies; see, e.g., Balokovic et al. 2016; Acciari et al. 2021) in Eq. (6). Consequently, this yields a range of upper limits between 1.3×10^{16} cm and 1.1×10^{18} cm for the emission zone responsible for that extreme variability. Several of these instances included the 0.3–100 GeV IDVs which occurred in Periods 1–2 and 5. Totally, we detected 25 IDVs from the LAT observations of Mrk 421 with $F_{\text{var}} = 36.7(10.5)–90.0(19.8)$ per cent from the robust detections of the source (with $TS \geq 9$ and $N_{\text{pred}} \geq 8$), and a vast majority of these instances belongs to Periods 1–2 and 6. Note that only one out of these IDVs (occurring in 2013 April) was reported within the past studies (see Kapanadze et al. 2016), and Mrk 421 is the only HBL source which has shown a LAT-band IDV (owing to the general presence of the higher-energy SED peak beyond the LAT range, contrary to the LBL and IBL objects). The highest-amplitude 0.3–300 GeV IDV was associated with the brightness drop by a factor more than 3.2 (taking the error ranges into account; on 2022 May 8, Period 6), whereas the fastest instance was recorded on 2013 July 15 (during the unprecedented X-ray and TeV-band outbursts): after reaching the highest historical level of $10^{-7} \text{ph cm}^{-2} \text{s}^{-1}$, the 0.3–300 GeV bright-

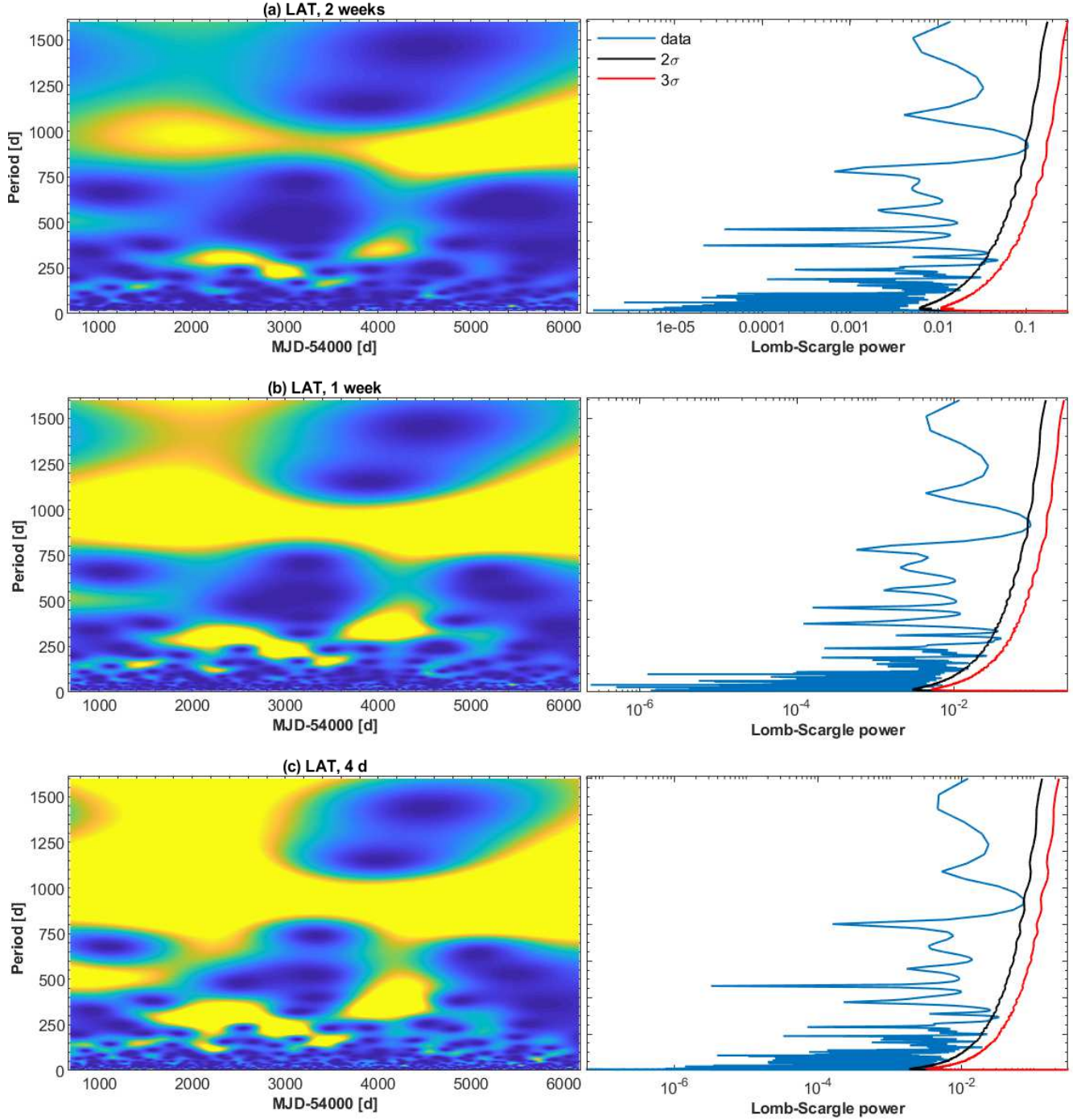


Fig. 7 The WWZ (left column) and LSP (right column) plots from (1) the LAT observations during 2008–2023, based on the 0.3–300 GeV flux values derived via the different time integrations.

ness practically halved within the next 2 hr. However, these instances were significantly less extreme compared to those recorded in the X-ray and TeV energy ranges (generally containing the lower- and higher-energy SED peaks of Mrk 421). For example, the VHE flux increased by a factor of 20–25 in about 0.5 hr (Gaidos et al. 1996). The source varied within the time intervals as short as a few hundred second in the 0.3–

10 keV band and showed a flux doubling/halving instances down to 1 hr in 2013 April (Kapanadze et al. 2016) etc.

5.2 Particle acceleration and cooling

As discussed in Section 3.1, the 0.3–300 GeV light curves were characterized by a variety of flare pro-

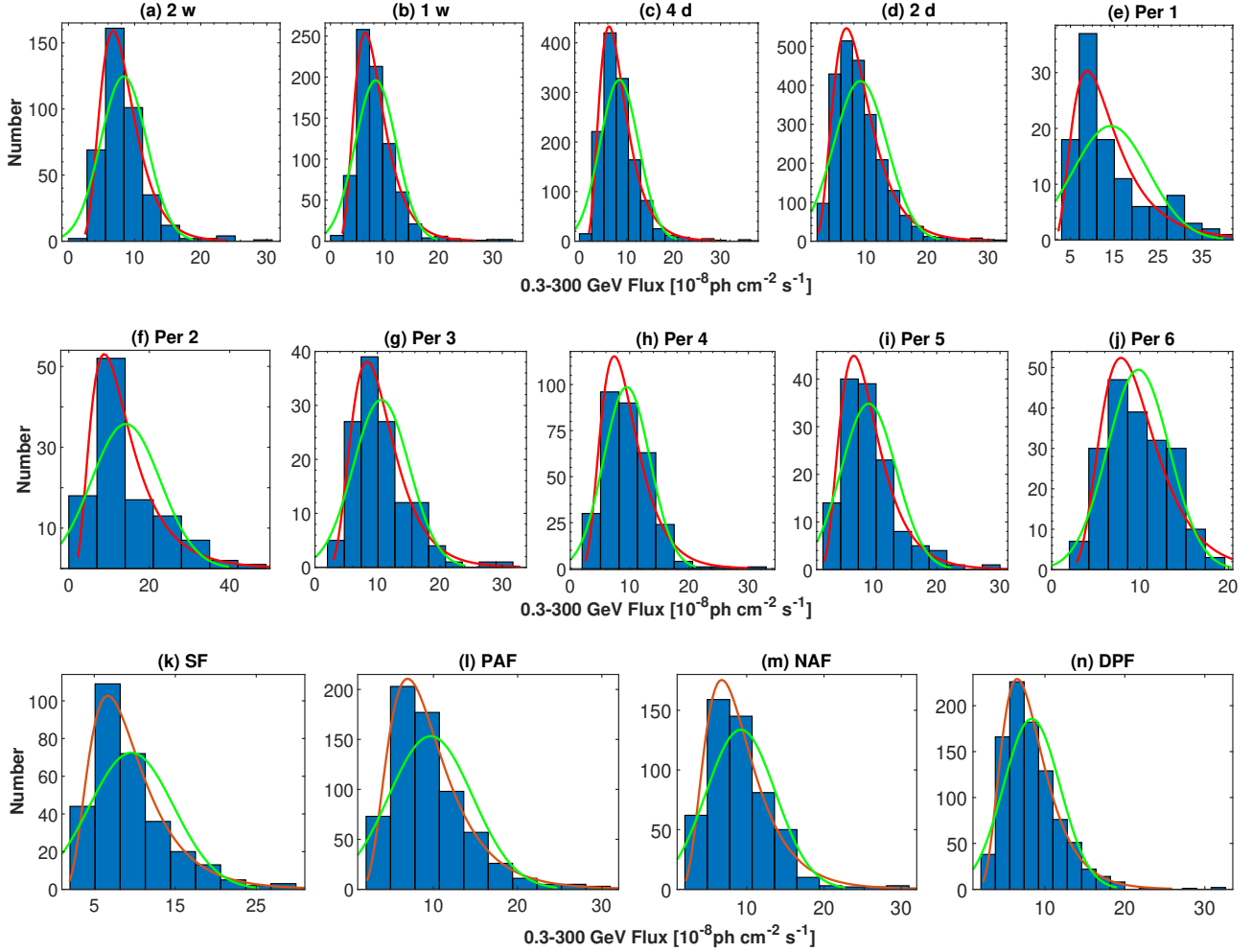


Fig. 8 Distribution of the LAT-band flux values from the different time integrations during 2008–2023 [panels (a)–(d)] and that from the 2-d binned data for different periods [panels (e)–(j)], as well as for those time intervals showing the LAT-band flares of Mrk 421 with different profiles [panels (k)–(n); SF – symmetric flares, PAF – positively-asymmetric flares, NAF – negatively-asymmetric flares and DPF – double-peak flares]. The red and green curves show the lognormal and Gaussian fits to the histograms, respectively.

files (symmetric, two-peak, positive or negative asymmetry). Different studies showed that the specific cases of the interplay between the particle acceleration and cooling can yield a characteristic profile of the particular flare. First of all, a symmetric profile can be determined by the light travel time effects, while the particle acceleration and cooling timescales (in the given spectral range) are much shorter than the light-crossing timescale (Finke 2024). This means that these timescales were much shorter than the light-crossing time the LAT-band emission zone for the (quasi)symmetric flares presented in Table 3.

Alternatively, a symmetric shape of the flare (with a possible plateau) indicates that the observed variability was driven by the crossing time-scale of the underlying disturbance, e.g., a shock front (Roy et al. 2019). Moreover, relativistic magnetic reconnection in

blazar jets can produce “plasmoids”, i.e., “blobs” of magnetized, nonthermal plasma of various sizes, which contain high-energy particles capable of upscattering lower-energy photons to the γ -ray energy range (see, e.g., Petropoulou et al. 2015, 2016). According to time-dependent modeling of emission from these extreme jet structures, the plasmoid-powered γ -ray flares (e.g., in the LAT energy range) can be observed as symmetric in the case the plasmoids are not changing in size rapidly (Christie et al. 2019; Mayer et al. 2021). It is important that a hard or very hard power-law electron energy distribution (EED) $N(\gamma \propto \gamma^{-p})$ can be established by the relativistic reconnection operating in the magnetized jets areas, characterized by $p \rightarrow 1$ when the photon index $\Gamma \lesssim 1.5$ and the upstream magnetization $\sigma_{\text{up}} \gtrsim 10$ (see, e.g., Sironi & Spitkovsky 2014).

Table 11 List of the time intervals characterized by spectral softening at the GeV energies (extract). Columns 2–4 present the number of the model-predicted photons, test-statistics and photon-index value in the 0.3–1 GeV band, whereas the same quantities from the 1–10 GeV and 10–300 GeV bands are provided in the Columns 5–7 and 8–10, respectively.

Dates/MJDs (1)	0.3–1 GeV			1–10 GeV			10–300 GeV		
	N_{pred} (2)	TS (3)	Γ (4)	N_{pred} (5)	TS (6)	Γ (7)	N_{pred} (8)	TS (9)	Γ (10)
2009 May 12—Jun 8/(549)63–90	157	342	1.53(0.10)	114	705	1.93(0.12)	23	303	1.78(0.10)
2009 Jul 7—Aug 4/(550)19–46	82	124	1.59(0.19)	91	578	1.57(0.09)	10	174	2.68(0.20)
2009 Dec 22—2010 Jan 18/(55)187–214	145	372	1.36(0.15)	122	879	1.43(0.08)	24	258	1.69(0.10)
2010 Jan 19—Feb 15/(552)15–42	88	229	1.27(0.20)	121	888	1.53(0.05)	15	195	1.71(0.11)

We have checked that the source showed very and extremely hard LAT-band spectra during some symmetric flares. This especially was the case during the shorter-term instances lasting several days [e.g., those occurring during MJD (548)46–52, (553)25–31 and (572)33–40] when only very and extremely hard LAT-band spectra were observed. These flares could be produced by those plasmoids containing very energetic plasma and characterized by slow change in size. Note that Kapanadze et al. (2024) presented a number of the detections of the reconnection-related features from the X-ray spectral study of mrk 421, which belong to each period discussed in Section 3.2. However, other instances also include softer spectra or are exceedingly long to be triggered only by the RMR, and could be affected by the light time travel effects. Finally, log-parabolic spectra were also observed during some symmetric flares. Such spectra can be established within the energy-dependent acceleration probability process (EDAP), which represents a variety of the first-order Fermi mechanism operating at the relativistic shock front (Massaro et al. 2004 and references therein): electrons can be confined by a magnetic field at the shock front, while the confinement efficiency is dropping with increasing lepton’s energy (Otherwise, the establishment of power-law EEDs are expected). Moreover, the logparabolic EEDs can be established by the stochastic acceleration, which can be efficient in the jet area with strong magnetic turbulence. The latter can be strongly enhanced after the passage of a relativistic shock in the magnetised, inhomogeneous jet medium (Marscher 2014). Different observational features, demonstrating the importance of both processes, have been reported by various authors from intense X-ray spectral studies, covering most of the periods discussed in Section 3.1 (e.g., Tramacere et al. 2009; Kapanadze et al. 2016, 2017a, 2018a,b, 2020, 2024). Therefore, some symmetric flares could be driven by the time-scale required for a relativistic shock front to cross that jet area, which was characterized by those physical properties required for electron acceleration to the energies

sufficient to upscatter low-energy photons to the MeV–GeV energies.

Moreover, a symmetric flare profile can be the result of the superposition of several episodes of short duration (Abdo et al. 2010b), and each one may be related to the different aforementioned processes. Finally, extremely hard LAT-band spectra could be the result of the significant contribution from the photons produced in the framework of the different hadronic processes (see the discussion below). Among the different periods, the symmetric LAT-band flares were the most frequent in Period 6 (four flares), leading to the suggestion that they were relatively favourable in point of the physical conditions yielding such instances. On the contrary, Period 5 was notable for the least occurrence of symmetric flares (only one instance in each). Note that the 0.3–300 GeV flux showed a lognormal variability during the symmetric flares, and the distribution of the corresponding photon-index values does not show a large difference from the Gaussian distribution (see Figures 6g and 8k). This result leads to the suggestion that these flares were predominantly controlled by the shock crossing time-scales and affected significantly by random fluctuations in the particle acceleration rate. These fluctuations could be caused by the subsequent shock passage through the jet area with different magnetic field properties (as discussed above). On the contrary, such distributions are lesser expected within the the plasmoid-related processes triggered by the local, pure jet-related instabilities.

Along with absence of the suitable physical conditions, the observation of symmetric flares is limited in the framework of the multi-zone emission scenarios: in the case the different emission regions are situated at different azimuthal angles in the jet cross-section and even each produce a symmetric flare, one could observe an overall asymmetric variability profile after the superposition of these emissions (Nalewajko 2013). Namely, the time-dependent modeling of Saito et al. (2015) demonstrated that a significant non-uniformity

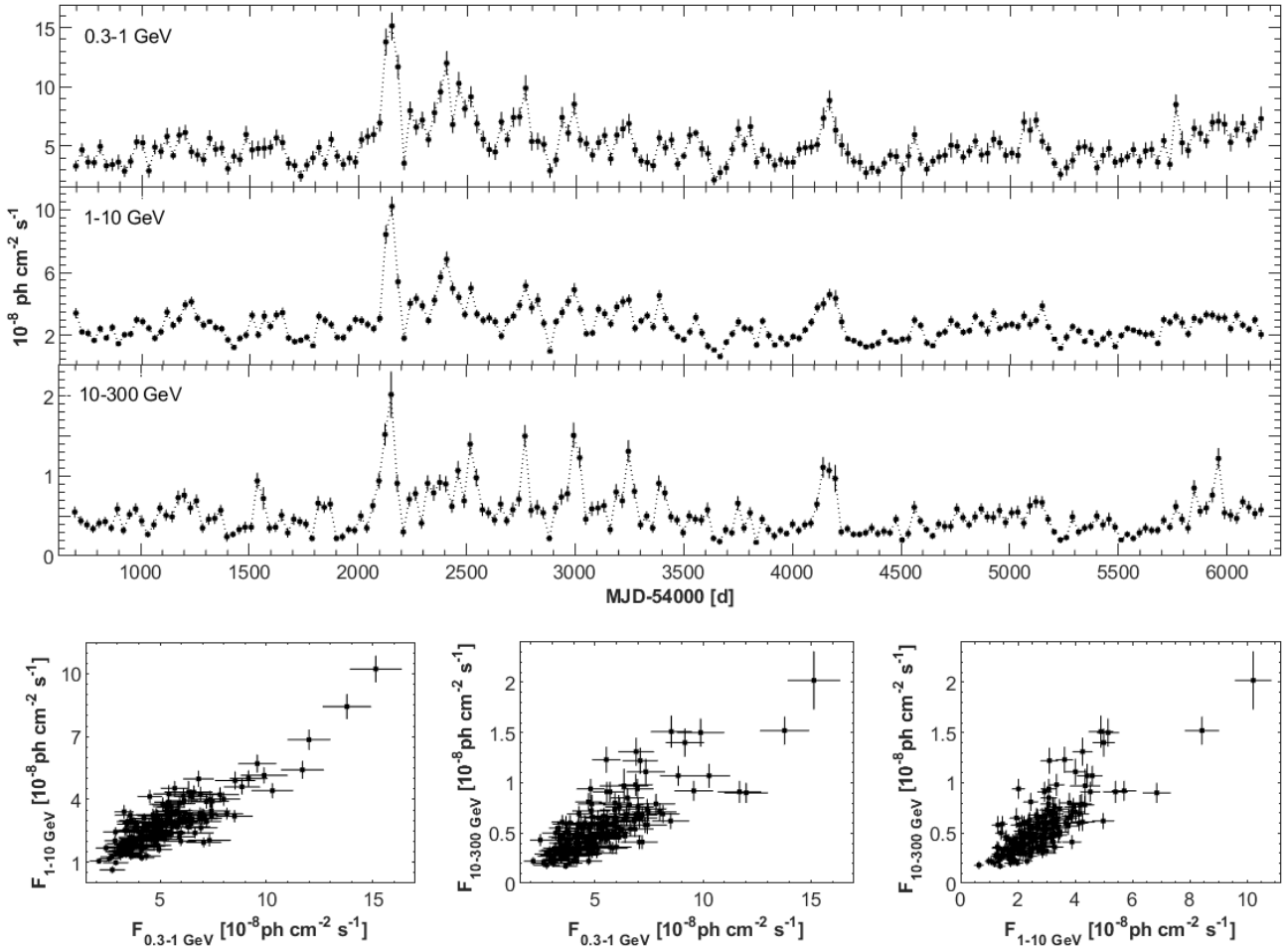


Fig. 9 Top: Light curves of Mrk 421 in the separate 0.3–1 GeV, 1–10 GeV and 10–300 GeV bands during 2008 August–2023 August, extracted with four-weekly integrations; bottom: correlations between the 0.3–1 GeV, 1–10 GeV and 10–300 GeV fluxes.

of the Doppler factor across the jet (caused by the radial expansion of the flow at the emission zone and boosted by the relativistic effects) can yield a significant symmetry distortion of the observed light curves and produce an positively-asymmetric flare profile with substantially extended brightness declining phase: since the emitting “shells” are considerably extended in the jet radial direction, their different parts are observed at different viewing angles. Consequently, the emission produced within those parts characterized by the largest inclinations arrive to the observer with a significant time delay compared to the emission situated at smaller viewing angles. In such a situation, the light curve corresponding to this phase can be less impacted by the radiative cooling of the highest-energy particles and will be dependent on the gradient of the bulk Doppler factor across the emitting shells. We suggest that this effect could be especially important during the periods notable for a lack of symmetric flares.

However, the variance of the Doppler factor across the emitting shell becomes smaller with the decreasing jet opening angle. Consequently, the flare asymmetry also decreases and is expected to become symmetric for the jet opening angle $\theta \lesssim 0.3 \text{ deg}$. Although Weaver et al. (2022) obtained a large value of the jet opening angle from the VLBA observations of Mrk 421 at 43 GHz ($\sim 55 \text{ deg}$), this result was mostly due to the projection effects caused by the very small angle to our line-of-sight (estimated to be $\sim 1.4 \text{ deg}$). The de-projected value, based on the method of Jorstad et al. (2017), yields $\theta \sim 1.4 \text{ deg}$ which is lower than the aforementioned threshold. Nevertheless, the jet of Mrk 421 is expected to be significantly narrower at the location of the γ -ray emission zone (situated much closer to the central SMBH than those jet parts emitting at 43 GHz). Moreover, the jet width at this location is possibly variable from epoch to epoch, becoming narrower than the aforementioned threshold and allowing us to observe symmetric LAT-band flares during some time intervals.

Alternatively, the origin of positively-asymmetric flares can be related to a fast injection of accelerated particles and slower radiative cooling and/or escape from the energization region. Consequently, such instances should be governed by Fermi-I acceleration at the relativistic shock front. Note that the distribution the 0.3–300 GeV flux values and photon-index from the corresponding time intervals are in favour of this possibility (see Figures 6h and 8l). On the other hand, the radiative lifetimes corresponding to the MeV–GeV energy range are generally very short. When the emitting shells are not considerably extended in the jet radial direction during the particular flare, the observed flare profile with an apparent positive asymmetry can be produced by the superposition of two or more low-amplitude, shorter-term events occurring during the long-term brightness decline (Roy et al. 2019). Note that the LAT-band flares with a positive asymmetry were relatively numerous in Period 5, characterized by a lack of symmetric flares. The latter results could be related to the superposition of lower-amplitude symmetric flares, producing a single, brightness-declining profile with a significantly longer duration compared to the brightness-increase phase. For example, strongly asymmetric flares frequently showed a subsequent secondary maximum after the peak brightness (see Figure 3B). According to Nalewajko (2013), the emitting region situated at the same distance across the jet, but oriented at a smaller angle to our line-of-sight, is located closer to the observer. Consequently, the light travel time is shorter for the emission from this region and is more strongly Doppler boosted compared to that from the region situated at larger distance from the jet axis. Therefore, one can observe a major peak followed by the minor one. Note that this scenario also can yield the distribution presented in Figure 8l, since the superposing symmetric flares could be governed by the shock-crossing timescale and show a lognormal flux distribution (as discussed above).

On the contrary, flares with a negative asymmetry may indicate a gradual acceleration of the electrons responsible for the IC upscattering of low-energy photons to the MeV–GeV range: the cooling time-scale of these particles can be shorter than the acceleration one (Roy et al. 2019). As mentioned above, a gradual electron acceleration is found to be inherent to the stochastic mechanism operating in the jet region with a low magnetic field and high matter density. Note that the negatively-asymmetric flares occurred in all periods, hinting at the importance of the stochastic particle acceleration [as reported by Kapanadze et al. (2016, 2017a, 2018a,b, 2020, 2024) from the intense X-ray spectral study]. On the other hand, the observation

of longer rising phase of the flares can be simply due to the superposition of two or more low-amplitude and short symmetric instances, not individually detectable but producing an apparently prolonged rising phase of a single flare (see Roy et al. 2019). Note that the flux and photon-index distributions from the time intervals of negatively-asymmetric flares (Figures 6i and 8m) hint at the viability of both these scenarios (strong turbulence due in the shocked jet area and γ -ray flare controlled by shock-crossing timescale).

Finally, the source also exhibited a two-peak flare profile 36 times in the LAT-band, which were observed during all here-discussed periods. According to the semi-analytic internal-shock model of Böttcher & Dermer (2010), two-peak flares can be related to the propagation of forward and reverse shocks. Namely, the central engine is considered to eject intermittently "shells" of high-energy, relativistic plasma at varying speeds through the blazar jet, which subsequently collide. Consequently, two different shocks may appear: a forward shock moving into the slower shell and a reverse one propagating in the faster shell. According to these simulations, (i) the higher-energy end synchrotron peaks, established directly behind the forward and reverse-shock fronts, remains essentially unaffected as long as the observer receives synchrotron emission from the shocks still being located within the shells; (ii) as the forward and reverse shocks propagate, an increasingly larger region of the shells is energized with particles having longer time to cool. Consequently, the synchrotron spectrum extends progressively from X-ray to UV and lower frequencies; (iii) as one observes the shock regions leaving the shells, the highest-energy electrons rapidly cool and leading to the decline in the high-frequency synchrotron emission. One expects a delayed response of the SSC component with respect to the X-ray emission, with slightly cooled electrons still being able to efficiently upscatter synchrotron "seed" photons up to γ -ray energies in the Thomson regime. Note that this scenario frequently was the case for the two-peak flares presented in Table 3 (see also the MWL light curves from different periods in Figure 2).

Since the emergence of colliding plasma shells could be caused by those unstable processes which operate in the innermost AD parts, the resulted double-peak flares should show their imprint on the target's jet. Actually, the distribution of the corresponding 0.3–300 GeV flux values clearly prefer the lognormal function (see Figure 8n and Table 6). Moreover, some double-peak flares could be simply a superposition of two separate LAT-band flares, the origin of which were not related to the colliding shells but to some processes capable for yielding a lognormal variability (as discussed above).

For example, a subsequent passage of single relativistic shock (triggered by the AD instabilities) through those jet inhomogeneities, which were characterized by different sizes and magnetic field properties but situated relatively closely to each other. Consequently, two separate flares with similar or different profiles (symmetric, positive or negative asymmetry) could occur, which overlapped each other and observed as a single double-peak flare. Eventually, the corresponding fluxes would also follow the lognormal distribution (as presented in Figure 8n). The distribution of the photon-index from the epochs of double-peak flares is different from the Gaussian function, to be observed within the dominance of a single process (random fluctuations in the particle acceleration rate; see Figure 6j).

5.3 Origin of the hard LAT-band spectra

As noted above, very and extremely hard γ -ray spectra are most commonly explained to have a hadronic origin (see, e.g., Mannheim 1993; Shukla et al. 2015). Accelerated leptons and hadrons are injected in the emitting region, which is uniformly filled with a magnetic field of strength B . These assumptions are in accord with the one-zone SPB model: all radiation mechanisms are operating in the same emission zone and external photon fields are negligible (see, e.g., Cerruti et al. 2020). The proton-proton interactions are thought to be negligible in the SPB models, since this mechanism requires very high particle density and the extreme jet powers for producing a significant γ -ray emission (Sol & Zech 2022). Table 9 presents the time intervals characterized by harder spectra in the 10–300 GeV energy range and explained by the significant contribution from the photons emitted in the framework of the proton-induced hadronic cascades (generally characterized by timing/spectral variability on longer timescales; see, e.g., Shukla et al. 2015; Sol & Zech 2022).

On the other hand, these instances can be explained within the framework of modified the one-zone SSC model of Zech & Lemoine (2021), which assumes that electrons are co-accelerated with protons by relativistic recollimation shocks under physical situations as follows: (1) low jet magnetization and (2) electrons can be preheated in the shock transition layer, yielding relatively large minimum Lorentz factors when involved in the Fermi-I process. The latter can produce high-energy electron populations characterized by a large range of power-law indices down to very hard ones ($p \simeq 1$), depending on the properties of magnetic field and turbulence, shock speed and obliquity (Summerlin & Baring 2012). Namely, oblique, relativistic shocks (referred to as "superluminal", implying

that they cannot be the sites via the mutual Fermi-I mechanism) can energize charged particles via shock-drift acceleration (SDA; Begelman & Kirk 1990 and references therein), which is also known as fast Fermi process: particles are allowed to boost their energy by an order of magnitude even during a single shock encounter (Sol & Zech 2022). When the MHD turbulence is relatively weak, the SDA is the most efficient and can produce very or extremely hard EEDs (see, e.g., Sironi & Spitkovsky 2013). However, the γ -ray emission from the accelerated proton population (with the same number density as the electrons) should not make a significant contribution in the total energy "budget".

Note also that the photon-photon absorption process can yield arbitrarily hard spectra, if the γ -ray emission passes through the medium containing a hot photon gas with a narrow energy distribution characterized by $E_\gamma \epsilon_0 \gg m_e c^2$ (Aharonian et al. 2008): the medium becomes optically thick at the lower γ -ray energies and thin at higher one (due to the decrease in the cross-section of the $\gamma\gamma$ interaction). Consequently, intrinsically hard γ -ray spectra can be established. Moreover, Lefa et al. (2011) presented a time-dependent SSC model where extremely hard electron distribution is achieved within the stochastic acceleration of electrons producing a steady-state, relativistic Maxwellian (RM) particle distribution. The latter represents a time-dependent solution of the Fokker-Plank equation that incorporates the adiabatic and radiative energy losses of accelerating particles. Depending on the physical conditions in the jet emission zone (e.g., if particles undergo cooling beyond the acceleration zone, or the jet medium is clumpy), the combination of different pile-up distributions are capable of interpreting the observed γ -ray spectra. Shukla et al. (2016) presented a two-zone SSC scenario for the very and extremely hard LAT-band spectra of the HBL source Mrk 501, incorporating (1) a slowly-variable shock-in-jet component producing the underlying softer spectrum through the Fermi-I first process and (2) fastly variable, very hard component produced by intermittent injection of sharply peaked RM-type EED originating from the jet base. The latter could be established through stochastic acceleration from randomly moving Alfvén waves. This physical situation could be sometimes the case for also Mrk 421 when exhibiting very and extremely hard gamma-ray spectra. Moreover, very and extremely hard power-law spectra can be established by the RMR. Note that the importance of stochastic electron acceleration and RMR in the jet of Mrk 421 is reported in our previous studies and discussed in Sections 5.1–5.2.

The source showed large changes of the spectral hardness many times, with the most extreme hardenings and subsequent softenings with $\Delta\Gamma > 1$ during a

few days. These instances (as well as those observed on longer timescales) were generally associated with the emergence of the extremely hard spectra. The latter could have been established by the turbulence-driven RMR, while the turbulence had been strongly enhanced by the shock passage through the magnetized jet medium. On the other hand, small-scale strong turbulence could produce the spectral transitions power-law \rightarrow logparabolic \rightarrow power-law, which were shown by the source many times during the 15-yr period. Some other fast hardenings/softenings could be established by the subsequent emergence of the plasmoids corresponding to the relativistic and non-relativistic (yielding softer power-law spectra; French et al. 2023) magnetic reconnections in the γ -ray emission zone.

6 Summary

In this paper, we have presented the results from the detailed timing and spectral study of the nearby HBL source Mrk 421, based on the data obtained from the practically uninterrupted 15-yr *Fermi*-LAT observations during 2008 August–2023 August. The experimental results are compared with those obtained within different theoretical studies that made us capable of drawing conclusions about unstable physical processes operating in the jet emission zone and possible hadronic contribution to the observed HE emission. For this purpose, we also examined the interplay between the LAT-band flux variability and those observed in the VHE γ -rays (the data obtained with FACT and various Cherenkov-type telescopes), X-rays (XRT, BAT and MAXI), optical–UV (UVOT and ground-based telescopes) and radio (UMRAO, VLBA) energy ranges. Our basic experimental results and the underlying plausible physical processes can be summarized as follows:

- During the 15-yr period, Mrk 421 was the brightest LAT-band source among HBLs and detectable down to intraday timescales during the strong HE flares. The mean 0.3–300 GeV photon flux was about $7 \times 10^{-8} \text{ ph cm}^{-2} \text{ s}^{-1}$, attained the maximum value of $\sim 10^{-6} \text{ ph cm}^{-2} \text{ s}^{-1}$ during the two subsequent 1-hr segments during the 2013 April outburst and frequently was brighter than $10^{-7} \text{ ph cm}^{-2} \text{ s}^{-1}$ (observed very rarely for other HBLs).
- The source showed non-periodical brightness changes on various timescales. The longest-term variability was related to the baseline 0.3–300 GeV brightness change from several to yearly timescales, superimposed by shorter-term flares lasting from about one week to almost 4 months. Depending on the baseline flux variability and the strength of flaring, we

discerned six periods of the stronger 0.3–300 GeV flaring activity. The variable baseline brightness was superimposed by 32 symmetric and 37 two-peak flares (during the entire 2008–2023 period), as well as by those having positive and negative asymmetries (42 and 37 instances, respectively), characterized by fractional amplitudes $F_{\text{var}}=15.5(5.1)–72.7(7.8)$ per cent. The strongest MeV–GeV flaring activity of Mrk 421 was recorded during 2012 June–2013 October and 2017 October–2018 March. Our study revealed 175 instances of 0.3–10 GeV flux doubling/halving with the corresponding timescales $\tau_{\text{d,h}}$ ranging from 5 hr to ~ 17.5 d and generally associated with short-term flares. These instances allowed us to constrain the upper limit to the emission zone size as $1.3 \times 10^{16} \text{ cm}–1.1 \times 10^{18} \text{ cm}$ by assuming a Doppler factor of 25. Several out of these instances included the 0.3–10 GeV IDVs, the total number of which amounted to 25 and were characterized by $F_{\text{var}}=36.7(10.5)–90.0(19.8)$ per cent.

- Disparate flare profiles are related to the different interplays between the light-crossing, particle acceleration and cooling timescales. Symmetric flares are governed by the light time travel effects or by the crossing time-scale of the underlying disturbance, as well as could be produced by the reconnection-born plasmoids not changing in size rapidly. Relatively long symmetric flares can be the result of the superposition of several episodes of short duration. However, when the different emission regions are situated at different azimuthal angles in the jet cross-section and even each produce a symmetric flare, one can observe a positively-asymmetric flare profile. Alternatively, the origin of positively-asymmetric flares can be related to a fast injection of accelerated particles and slower radiative cooling and/or escape from the energization region. On the contrary, flares with a negative asymmetry may indicate a gradual acceleration of the electrons responsible for the IC upscattering of low-energy photons to the MeV–GeV range: the cooling time-scale of these particles can be shorter than the acceleration one, hinting at the importance of the stochastic particle acceleration. The source also frequently exhibited two-peak flare profiles, plausibly triggered by the "shells" of high-energy, relativistic plasma moving with different speeds through the blazar jet and subsequently colliding.
- During the period of our study, the source underwent a lognormal variability in the LAT energy range, explained as an imprinting of the disc nonstationary processes on the jet (e.g. shock propagation through the jet, triggered by the multiplicative processes in

the disc innermost parts). Alternatively, the lognormal variability could be contributed also by proton-initiated hadronic cascades, the presence of which explains the observation of very hard LAT-band spectra and hardening beyond 10 GeV. Moreover, a lognormal flux variability was accompanied by the Gaussian distribution of the photon index during some periods, explained by random fluctuations in the particle acceleration rate (in turn, possibly due to the frequent random transitions from dominance of the first-order Fermi process to that of stochastic acceleration and vice versa). Short-term LAT-band flares were frequently observed in the epochs of the X-ray flaring activity, hinting at the connection between these instances, e.g., via the IC-upscatter of the X-ray photons in the KN-regime. The latter explains a spectral softening at the energies beyond 1 GeV or 10 GeV compared to the lower-energy part of the spectrum during some time intervals and attenuation of the expected strong correlation between the fluxes extracted in these bands.

- Most of the 0.3–300 GeV spectra were well-fit with a simple power-law model and showed a very broad range of the photon-index from $\Gamma \sim 2.8$ down to $\Gamma \sim 1.2$, with the mean values $\Gamma_{\text{mean}} = 1.75(0.01) - 1.84(0.01)$ and distribution peaks $\Gamma_p = 1.73(0.01) - 1.82(0.01)$. The source showed large changes of the spectral hardness changes, with the most extreme hardenings and/or softenings with $\Delta\Gamma > 1$ during 2–5 days, generally associated with the emergence of the extremely hard spectra. The latter could be established by the turbulence-driven RMR, by the SDA at recollimation shocks or by the subsequent emergence of the plasmoids corresponding to the relativistic and non-relativistic magnetic reconnections in the γ -ray emission zone. Strong small-scale turbulence could trigger the spectral transitions power-law \rightarrow logparabolic \rightarrow power-law, as well as produce very logparabolic spectra with a wide range the photon index down to $\alpha \sim 1$. The hardenings, observed on relatively longer timescales during those time intervals characterized by harder spectra in the 10–300 GeV energy range could be associated to the proton-induced hadronic cascades.

7 Acknowledgements

BK and AG thank Shota Rustaveli National Science Foundation and E. Kharadze National Astrophysical Observatory (Abastumani, Georgia) for the fundamental research grant FR–21–307. We acknowledge the use of public data from the *Swift* data

archive. This research has made use of the XRTDAS software, developed under the responsibility of the ASDC, Italy. We acknowledge the use of the VHE data from long-term Whipple observations and the variable star observations from the AAVSO International Database contributed by observers worldwide and used in this research. The observational program at UMRAO was supported in part by a series of grants from the NSF, most recently AST 0607523, and by a series of grants from the NASA Fermi Guest Investigator program NNX 09AU16G, NNX10AP16G, NNX11AO13G, and NNX13AP18G. This study makes use of VLBA data from the VLBA-BU Blazar Monitoring Program (BEAM-ME and VLBA-BU-BLAZAR; <http://www.bu.edu/blazars/BEAM-ME.html>), funded by NASA through the Fermi Guest Investigator Program. The VLBA is an instrument of the National Radio Astronomy Observatory. The National Radio Astronomy Observatory is a facility of the National Science Foundation operated by Associated Universities, Inc. Finally, we thank the anonymous referee for his/her useful suggestions.

References

- Abdo, A. A., et al. 2009a, *Astrophys. J. Suppl. Ser.*, 183, 46
- Abdo, A. A., et al. 2009b, *Astrophys. J.*, 707, 1310
- Abdo, A. A., et al. 2010a, *Astrophys. J.*, 716, 30
- Abdo, A. A., et al. 2010b, *Astrophys. J.*, 722, 520
- Abdo, A. A., et al. 2011a, *Astrophys. J.*, 736, 131
- Abdo, A. A., et al. 2011b, *Astrophys. J.*, 727, 129
- Abe, S. et al. 2024, *Astron. Astrophys.*, 684, 127
- Abeysekara, A. U., et al. 2017, *Astrophys. J.*, 834, 2
- Acciari, V.A. et al. 2011, *ApJ*, 738, 25
- Acciari, V.A. et al. 2014, *Astropart. Phys.* 54, 1
- Acciari, V.A. et al. 2021, *Astron. Astrophys.*, 655, A89
- Aharonian, F. 2000, *New Astron.* 5, 377
- Aharonian, F., Khangulyan, D., & Costamante, L. 2008, *Mon. Not. R. Astron. Soc.*, 387, 1206
- Aharonian, F. et al. 2009, *Astron. Astrophys.*, 502, 749
- Ahnen, M. L., et al. 2016, *Astron. Astrophys.*, 593, 91
- Alecsic, J., et al. 2015a, *Astron. Astrophys.*, 576, 176
- Alecsic, J., et al. 2015b, *Astron. Astrophys.*, 578, 22
- Anderhub, H. et al. 2013, *Journ. of Instr.*, 8, article id. P06008
- Arbet-Engels, A. et al. 2021, *Astron. Astrophys.*, 647, 88
- Atwood, W. B., et al. 2009, *Astrophys. J.*, 697, 1071
- Balocovic, M., et al. 2016, *Astrophys. J.*, 819, 156
- Banerjee, B. et al. 2019, *Mon. Not. R. Astron. Soc.*, 487, 845
- Baring, M.G.; Böttcher, M.; Summerlin, E.J. 2017, *Mon. Not. R. Astron. Soc.*, 464, 4875
- Barthelmy, S. D., et al. 2005, *Space Sci. Rev.*, 120, 143
- Begelman M.C., & Kirk, J.G. 1990, *Astrophys. J.*, 353, 66
- Begelman, M.C., Fabian, A C., & Rees, M. J. 2008, *Mon. Not. R. Astron. Soc.*, 384, L19
- Bhatta, G. 2019, *Mon. Not. R. Astron. Soc.*, 2019, 487, 3990
- Bhatta, G., & Dhital, N. 2020, *Astrophys. J.*, 891, 120
- Biland, A. et al. 2014, *Journ. of Instr.*, 9, article id. P10012
- Blaziejowski, M., et al. 2005, *Astrophys. J.*, 630, 130
- Bondi, M. et al. *Mon. Not. R. Astron. Soc.*, 2001, 325, 1109
- Böttcher, M. 2007, *Astrophys. Space Sci.*, 309, 95
- Böttcher, M., & Dermer, C. 2010, *Astrophys. J.*, 711, 445
- Böttcher, M., et al. 2013, *Astrophys. J.*, 768, 54
- Böttcher, M., & Baring, M. G. 2019, *Astrophys. J.*, 887 133
- Burrows, D. N., et al. 2005, *Space Sci. Rev.*, 120, 165
- Carnerero, M. I., et al. 2017, *Mon. Not. R. Astron. Soc.*, 472, 3789
- Celotti, A., & Ghisellini, G. 2008, *Mon. Not. R. Astron. Soc.*, 385, 283
- Cerruti, M. I., et al. 2015, *Mon. Not. R. Astron. Soc.*, 448, 910
- Cerruti, M. I., et al. 2020, *Galax.* 8, 72
- Christie, I. M., Petropoulou, M., Sironi, L., & Giannios, D. 2019, *Mon. Not. R. Astron. Soc.*, 482, 65
- Di Gesu, L. et al. 2022, *Astrophys. J.*, 938, 7
- Dorner, D., Ahnen, M. L., Biland, A., et al. 2015, preprint (arXiv:1502.02582)
- Emmanoulopoulos, D., McHardy, I. M., & Papadakis, I. E. 2013, *MNRAS*, 433, 907
- Falomo, R., Pian E., & Treves A. 2014, *A&AR*, 2014, 22, 37
- Finke, J. 2013, *ApJ*, 763, 134
- Finke, J. 2024, *Front. Astron. Space Sci.*, 11:1384234
- Foster, G. 1996, *Astron. J.*, 112, 1709
- French, O., Guo, F., Zhang, Q. & Uzdensky, D. 2023, *Astrophys. J.*, 948, 19
- Gaidos, J., Akerlof, C. W., Biller, S., et al. 1996, *Nature*, 383, 319
- Gehrels, N., et al. 2004, *Astrophys. J.*, 611, 1005
- Giebels, B., & Degrange, B. 2009, *Astron. Astrophys.*, 503, 797
- Grossmann, A., & Morlet, J. 1984, *SIAM J. Math. Anal.*, 15, 723
- Horan, D., Acciari, V. A., Bradbury, S. M., et al. 2009, *ApJ*, 695, 596
- Hovatta, T., et al. 2015, *Mon. Not. R. Astron. Soc.*, 448, 3121
- Jorstad, S., et al. 2017, *Astrophys. J.*, 846, 98
- Kapanadze, B., et al. 2016, *Astrophys. J.*, 831, 102
- Kapanadze, B., et al. 2017a, *Astrophys. J.*, 848, 103
- Kapanadze, B., et al. 2017b, *AIPC*, 1792, id.050021
- Kapanadze, B., et al. 2018a, *Astrophys. J.*, 854, 66
- Kapanadze, B., et al. 2018b, *Astrophys. J.*, 858, 68
- Kapanadze, B., et al. 2018c, *Astrophys. J. Suppl. Ser.*, 238, 13
- Kapanadze, B., et al. 2020, *Astrophys. J. Suppl. Ser.*, 247, 27
- Kapanadze, B., et al. 2023, *Astrophys. J. Suppl. Ser.*, 268, 20
- Kapanadze, B., et al. 2024, *Astrophys. J. Suppl. Ser.*, in press
- Kissaka, S.; Levinson, A.; Toma, K.; Niv, I. 2022, *Astrophys. J.*, 924, 28.
- Krimm, H. A., Holland, S. T., Corber, R. H. D., et al. 2013, *ApJ*, 209, 14
- Lefa, E.; Rieger, F.M.; Aharonian, F. 2011, *Astrophys. J.*, 740, 64
- Levinson, A., & Rieger, F. 2011, *Astrophys. J.*, 730, 123
- Lomb, N. R. 1976, *Astrophys. Space Sci.*, 39, 447
- Mannheim, K. 1993, *Astron. Astrophys.*, 269, 60
- Marscher, A. P., & Gear, W. K. 1985, *Astrophys. J.*, 298, 114
- Marscher, A. P. 2014, *Astrophys. J.*, 780, 87
- Massaro, E., et al. 2004, *Astron. Astrophys.*, 413, 489
- Matsuoka, M., et al. 2009, *Publ. Astron. Soc. Jpn.*, 61, 999
- Mayer, M., Petropoulou, M., and Christie, I. M. 2021, *Astrophys. J.*, 912, 40
- Moderski, R., Sikora, M., & Blaziejowski, M. 2003, *A&A*, 406, 855
- Nalewajko, K. 2013, *MNRAS*, 430, 1324
- O’Neil, S., Kiehlman, S., Readhead, A. C. S., et al. 2022, *ApJ*, 926, L35
- Padovani, P., & Giommi, P. 1995, *Astrophys. J.*, 444, 567
- Petropoulou, M., et al. 2015, *Mon. Not. R. Astron. Soc.*, 448, 2412
- Petropoulou, M., et al. 2016, *Mon. Not. R. Astron. Soc.*, 462, 3325
- Plotkin, R. M. et al. 2012, *ApJ*, 745, L27
- Rieger, F. M. 2019, *Galax.* 7, 28
- Roming, P. W. A., et al. 2005, *Space Sci. Rev.*, 120, 95
- Roy, N., Chatterjee, R., Joshi, M., & Ghosh, A. 2019, *MNRAS*, 743, 757
- Saito, S., et al. 2013, *Astrophys. J.*, 766, L11
- Saito, S., Stawarz, L., Tanaka, Y. K., et al. 2015, *ApJ*, 809, 171
- Scargle, J. D. 1982, *Astrophys. J.*, 263, 835

-
- Shukla, A., et al. 2012, *Astron. Astrophys.*, 541, 140
- Shukla, A., Chitnis, V. A., Singh, B. B., et al. 2015, *ApJ*, 798, 2
- Shukla, A., et al. 2016, *Astron. Astrophys.*, 591, 83
- Sikora M., Begelman M. C., Rees M. J., 1994, *Astrophys. J.*, 421, 153
- Sinha, A., et al. 2016, *Astron. Astrophys.*, 591, 81
- Sinha, A., Khatoon, R., Misra, R., et al. 2018, *MNRAS*, 480, L116
- Sironi, L., & Spitkovsky, A. 2013, *Astrophys. J.*, 771, 54
- Sironi, L., & Spitkovsky, A. 2014, *Astrophys. J.*, 783, L21
- Sokolov, A., et al. 2004, *Astrophys. J.*, 613, 725
- Sol, H.; Zech, A. 2022, *Galax.* 10, 105.
- Sobacchi, E., Sormani, M.C., & Stamerra, A. 2017, *Mon. Not. R. Astron. Soc.*, 465, 161
- Summerlin, E.J., & Baring, M.G. 2012, *Astrophys. J.*, 745, 63
- Tarnopolski, M., et al. 2020, *Astrophys. J. Suppl. Ser.*, 250, 1
- Tammy, J., & Duffy, P. 2009, *Mon. Not. R. Astron. Soc.*, 393, 1063
- Tavani, M.; Cavaliere, A.; Munar-Adrover, P.; Argan, A. 2008, *Astrophys. J.*, 854, 11
- Tramacere, A., et al. 2009, *Astron. Astrophys.*, 501, 879
- VanderPlas, J. T. 2018, *Astrophys. J. Suppl. Ser.*, 236, 16
- Vaughan, S., et al. 2003, *Mon. Not. R. Astron. Soc.*, 345, 1271
- Virtanen, J. J. P., & Vainio R. 2005, *Astrophys. J.*, 621, 313
- Weaver, Z. R., et al. 2022, *Astrophys. J. Suppl. Ser.*, 260, 12
- Zech, A., & Lemoine, M. 2021, *Astron. Astrophys.*, 654, 96

!Article title?

Author

Author

¹ Affiliation